Submitted to The Open Journal of Astrophysics
Preprint typeset using LaTeX style openjournal v. 09/06/15

arXiv:2610.08731v1 [astro-ph.CO] 6 Oct 2026

HALO MASS FUNCTION CONSTRAINTS ON EARLY GALAXY AND AGN POPULATIONS IN THE JWST ERA

Elan Yogeswaren
Terra Nova Sciences LLC, Houston, TX, 77054 USA

Robert K. Schaefer
Johns Hopkins University Whiting School EP Applied Physics Program and the Applied Physics Laboratory, Laurel, MD, 20723 USA

Preprint – 2026

ABSTRACT

The discovery by the *James Webb Space Telescope* (JWST) of massive galaxies and luminous active galactic nuclei (AGN) at high redshift provides an increasingly sensitive test of the connection between cosmological structure formation and the astrophysical processes that make dark-matter halos observable. We develop a unified framework connecting the linear matter power spectrum to the mass variance, peak height, halo mass function (HMF), cumulative halo abundance, and observable galaxy and AGN populations. We use the Sheth–Tormen (ST) HMF as the baseline and compare it with an illustrative Bolshoi/Klypin-calibrated modification (KST) to quantify the sensitivity of high-redshift predictions to the calibration of the HMF against cosmological N-body simulations. We apply the framework to three complementary tests: the baryonic and stellar-mass reservoir available to massive galaxies, the abundance of halos capable of hosting luminous AGN, and the rest-frame ultraviolet luminosity function of high-redshift galaxies. Because the most massive systems occupy the rare, high-peak tail of the halo distribution, modest changes in inferred host mass, baryonic conversion efficiency, black-hole occupation or duty cycle, and HMF calibration can produce large changes in predicted abundances. The ST–KST comparison shows that uncertainty in the high-redshift halo population can materially affect the inferred host supply, particularly toward $z \sim 10$, while leaving the underlying halo-to-observable mappings unchanged. Comparison with representative JWST massive-galaxy, AGN, and UV-luminosity-function measurements demonstrates that matching the properties of an individual source is not sufficient for population consistency: the corresponding host halos must also exist in adequate numbers. Current observations do not by themselves require a departure from standard ΛCDM, but they provide increasingly stringent quantitative stress tests of both cosmological halo abundances and the baryonic and black-hole physics connecting halos to observable sources at cosmic dawn.

1. INTRODUCTION

The large-scale structure of the Universe is understood to have arisen from the gravitational amplification of tiny primordial departures from exact homogeneity. In the standard cosmological picture, nearly scale-invariant, approximately Gaussian primordial perturbations evolved through the radiation- and matter-dominated eras and ultimately seeded the nonlinear dark matter halos that host galaxies and supermassive black holes. A successful description of early galaxy and active galactic nucleus (AGN) formation must therefore connect the primordial fluctuation field, its scale-dependent linear evolution, the nonlinear collapse of overdense regions, and the observable populations that occupy the resulting halos (Peebles 1980; Peacock 1999; Dodelson and Schmidt 2020; Planck Collaboration VI 2020).

This connection is conventionally constructed from the matter power spectrum. Transfer functions encode the scale-dependent evolution of primordial perturbations through radiation domination, matter–radiation equality and recombination, while the linear growth factor describes their subsequent redshift evolution (Bardeen *et al.* 1986; Eisenstein and Hu 1998; Peacock 1999; Dodelson and Schmidt 2020). Smoothing the resulting matter spectrum on a mass scale gives the variance $\sigma(M, z)$ and peak-height variable $\nu(M, z)$, which provide the statistical inputs to analytic halo-abundance models. Spherical-collapse theory, Press–Schechter theory, excursion-set methods and ellipsoidal-collapse extensions then provide a bridge from the linearly evolved density field to the abundance of gravitationally bound halos (Gunn and Gott 1972; Press and Schechter 1974; Bond *et al.* 1991; Lacey and Cole 1993; Sheth and Tormen 1999; Tinker *et al.* 2008).

The high-mass tail of this halo population is especially informative at early times. If an observed galaxy or AGN requires a halo above some characteristic mass, then the cumulative abundance of such halos limits the number of possible hosts. Because increasingly massive halos correspond to increasingly rare peaks at high redshift, observations of luminous galaxies and accreting black holes during the first billion years provide a sensitive test of the combined cosmological halo supply and the astrophysical processes that connect halos to observable systems (Kormendy and Ho 2013; Volonteri 2010; Inayoshi *et al.* 2020).

This issue has become particularly important with the *James Webb Space Telescope* (JWST). Deep imaging and spectroscopy have revealed substantial populations of luminous galaxies and candidate AGN at $z \gtrsim 6$, including objects whose inferred stellar masses, luminosities or black-hole properties make them demanding tests of early

structure and baryonic assembly (Labb
'e *et al.* 2023; Boylan-Kolchin 2023; Atek *et al.* 2023a,b; Harikane *et al.* 2023; Kocevski *et al.* 2023; Maiolino *et al.* 2024; Napolitano *et al.* 2025). At the population level, measurements of high-redshift rest-frame ultraviolet luminosity functions provide an additional constraint because a successful model must reproduce not only the luminosity of individual objects but also their observed number densities (Donnan *et al.* 2023, 2024; Franco *et al.* 2025).

The central organizing principle of the present work is therefore a number-density framework. For a chosen halo mass function (HMF) model X, we write

$$\frac{dn_X}{dM_h}(M_h, z), \tag{1}$$

for the differential comoving abundance of halos of mass M_h at redshift z. An observable population is then connected to this cosmological halo supply through an occupation or selection function,

$$n_{\mathrm{obj},X}(z) = \int_0^\infty \langle N_{\mathrm{obj}} \mid M_h, z\rangle \, \frac{dn_X}{dM_h}(M_h, z)\, dM_h. \tag{2}$$

Equation (2) is deliberately general. The HMF specifies how many halos cosmology provides, while $\langle N_{\mathrm{obj}} \mid M_h, z\rangle$ specifies how those halos are mapped into the observed population. This separation between *halo supply* and *halo-to-observable physics* is the common structure underlying the different tests developed below.

We apply this framework in three complementary ways. First, we construct a *baryonic-reservoir and massive-galaxy test*: the cosmic baryon fraction limits the stellar mass that can be assembled in halos of a given mass, while the cumulative HMF determines whether a sufficient number of such halos exists. Second, we construct an *AGN host-abundance test*: the available halo population is combined with a minimum host mass, black-hole occupation fraction and AGN duty cycle to constrain the number density of active systems. Third, we construct a *galaxy UV luminosity-function test*: a controlled stellar halo-to-light mapping converts halo mass into rest-frame UV magnitude, allowing the predicted population $\Phi(M_{\mathrm{UV}}, z)$ to be compared directly with high-redshift measurements. These tests probe related physics but should not be conflated. In particular, the stellar UV mapping used for the galaxy luminosity function is not an AGN luminosity model.

For the cosmological halo supply, the Sheth–Tormen (ST) mass function is used as the principal analytic baseline. We additionally examine the Bolshoi-calibrated Klypin modification of the ST abundance (Klypin *et al.* 2011). Recent high-resolution multi-scale simulations provide alternative HMF calibrations; for example, Benson *et al.* (2026) combine cosmological-volume and zoom-in simulations to construct a flexible HMF calibration spanning a broad range of halo masses and dark-matter power spectra. Such developments illustrate that the simulation calibration of the HMF remains an active area of research and provide complementary alternatives to the Bolshoi/Klypin prescription considered here. This Klypin-corrected Sheth–Tormen (KST) branch is not treated as a unique or definitive high-redshift HMF. Rather, it provides a controlled example of how a simulation-motivated change in halo abundance propagates through otherwise identical baryonic and occupation assumptions.

An important feature of this organization is that it separates questions that can otherwise appear degenerate. Increasing a stellar-conversion efficiency can make a halo more luminous, but it does not create additional halos. Changing an AGN duty cycle changes the fraction of eligible hosts observed in an active phase, but it does not change the cosmological abundance of those hosts. Conversely, changing the HMF alters the supply of halos without, by itself, changing the luminosity assigned to an individual halo. The framework therefore provides a direct way to identify whether an apparent high-redshift discrepancy is primarily associated with halo abundance, baryonic conversion, black-hole occupation and activity, or an observational mapping.

The purpose of this paper is to use the emerging JWST high-redshift populations as a quantitative stress test of standard ΛCDM structure formation and of the astrophysical assumptions that connect dark matter halos to observable galaxies and AGN. Rather than interpreting any apparent discrepancy as evidence for a failure of the standard cosmological model, we use a transparent analytic and numerical framework to quantify how demanding different high-redshift observations are under explicitly stated assumptions, and to examine how those conclusions change when the adopted halo abundance or halo-to-observable mapping is varied. This distinction is especially important because stellar masses, star-formation efficiencies, black-hole masses, Eddington ratios, occupation fractions, duty cycles, luminosity scatter, survey completeness, and cosmic variance can all influence the inferred level of tension.

2. COSMOLOGICAL AND HALO-MODEL INPUTS

The observational tests developed in this work require a common cosmological prediction for the abundance of dark-matter halos as a function of mass and redshift.

The calculation begins with the linear matter power spectrum, constructs the mass variance and peak-height parameter, and then uses these quantities to evaluate the halo mass function (HMF). The sequence may be summarized as

$$\begin{aligned} P_{\mathrm{m}}(k,0) \longrightarrow \sigma(M,0) \longrightarrow \sigma(M,z) \longrightarrow \nu(M,z) \\ \longrightarrow \frac{dn_X}{dM} \longrightarrow n_X(>M,z), \end{aligned} \tag{3}$$

where X denotes the adopted halo-abundance prescription. The Sheth–Tormen (ST) mass function provides the principal analytic baseline. Press–Schechter (PS) is included as the spherical-collapse reference, and a Bolshoi/Klypin-calibrated modification of ST is used to examine the sensitivity of the high-redshift predictions to the adopted HMF calibration.

2.1. *Fiducial Cosmology*

The critical density ρ_{crit} for a flat universe is defined as

$$\rho_{\mathrm{crit},0} = \frac{3H_0^2}{8\pi G}, \tag{4}$$

where H_0 is the present value of the Hubble constant, and G is Newton's gravitational constant.

We adopt a Planck-like, spatially flat ΛCDM cosmology (Planck Collaboration VI 2020). The principal parameters

are

$$\begin{aligned} \Omega_{\rm m} &\simeq 0.316, \quad \Omega_{\rm b} \simeq 0.0493, \\ h &\simeq 0.673, \quad n_{\rm s} \simeq 0.965, \\ \sigma_8 &= 0.812. \end{aligned} \tag{5}$$

where $\Omega_a = \rho_a/\rho_{\rm crit}$ denotes the density parameter of component a, and

$$h \equiv \frac{H_0}{100\,{\rm km\,s^{-1}\,Mpc^{-1}}}. \tag{6}$$

The parameter σ_8 is the rms linear matter fluctuation within spheres of radius $8\,h^{-1}\,{\rm Mpc}$ at $z = 0$. Spatial flatness gives

$$\Omega_\Lambda = 1 - \Omega_{\rm m} \simeq 0.684. \tag{7}$$

The numerical calculations use the corresponding fiducial parameter values with their full internal precision.

The mean comoving matter density is

$$\bar{\rho}_{\rm m} = \Omega_{\rm m}\rho_{\rm crit,0}. \tag{8}$$

The corresponding cosmic baryon fraction,

$$f_b = \frac{\Omega_{\rm b}}{\Omega_{\rm m}} \simeq 0.156, \tag{9}$$

sets the maximum baryonic reservoir associated with a halo and is an input for the massive-galaxy and luminosity applications developed below.

2.2. *Linear Matter Power Spectrum*

The present-day linear matter power spectrum is written

$$P_{\rm m}(k,0) = A_{\rm norm}\,k^{n_{\rm s}}T^2(k), \tag{10}$$

where $T(k)$ is the matter transfer function and $A_{\rm norm}$ fixes the overall normalization. The transfer function describes the scale-dependent processing of primordial density perturbations through the radiation- and matter-dominated eras. The numerical calculation uses the Eisenstein–Hu cold-dark-matter/baryon transfer-function prescription (Bardeen *et al.* 1986; Eisenstein and Hu 1998; Peacock 1999; Dodelson and Schmidt 2020; Mo *et al.* 2010).

The amplitude is normalized directly to the adopted value of σ_8. For a spherical top-hat filter of radius

$$R_8 = 8h^{-1}\,{\rm Mpc}, \tag{11}$$

the normalization condition is

$$\sigma_8^2 = \frac{1}{2\pi^2}\int_0^\infty k^2 P_{\rm m}(k,0)W^2(kR_8)\,dk. \tag{12}$$

Operationally, an unnormalized spectrum

$$P_{\rm unnorm}(k) = k^{n_{\rm s}}T^2(k) \tag{13}$$

is first used to calculate $\sigma_{8,\rm unnorm}$. The normalization is then

$$A_{\rm norm} = \left(\frac{\sigma_8}{\sigma_{8,\rm unnorm}}\right)^2, \tag{14}$$

so that

$$P_{\rm m}(k,0) = A_{\rm norm}P_{\rm unnorm}(k). \tag{15}$$

This procedure fixes the power-spectrum amplitude once and ensures that the spectrum used throughout the HMF calculation reproduces the specified σ_8.

2.3. *Linear Growth Factor*

The redshift evolution of the linear matter spectrum is described by the growth factor $D(z)$,

$$P_{\rm m}(k,z) = D^2(z)P_{\rm m}(k,0), \qquad D(0) = 1. \tag{16}$$

For the spatially flat matter–Λ background considered here, define

$$E(a) \equiv \frac{H(a)}{H_0} = \left[\Omega_{\rm m,0}a^{-3} + \Omega_{\Lambda,0}\right]^{1/2}. \tag{17}$$

The growing-mode solution may then be expressed as

$$D_+(a) = \frac{5\Omega_{\rm m,0}}{2}E(a)\int_0^a \frac{da'}{a'^3E^3(a')}, \tag{18}$$

with the normalized growth factor

$$D(a) = \frac{D_+(a)}{D_+(1)}, \qquad a = (1+z)^{-1}. \tag{19}$$

This form approaches the familiar matter-dominated behavior at high redshift while including the suppression of late-time growth by the cosmological constant (Peebles 1980; Peacock 1999; Dodelson and Schmidt 2020; Mo *et al.* 2010). The numerical calculation evaluates Equation (19) directly rather than imposing the Einstein–de Sitter approximation $D = (1+z)^{-1}$.

2.4. *Mass Variance and Peak Height*

The linear density field is smoothed on a comoving scale R using a spherical top-hat window. Its Fourier transform is

$$W(x) = \frac{3}{x^3}\left(\sin x - x\cos x\right), \tag{20}$$

with $x = kR$. The smoothing radius is related to the halo-mass coordinate by

$$M = \frac{4\pi}{3}\bar{\rho}_{\rm m}R^3. \tag{21}$$

The variance of the smoothed linear density field as a function of mass and redshift is

$$\sigma^2(M,z) = \frac{1}{2\pi^2}\int_0^\infty k^2 P_{\rm m}(k,z)W^2(kR)\,dk. \tag{22}$$

Since the adopted linear growth is scale independent,

$$\sigma(M,z) = D(z)\sigma(M,0). \tag{23}$$

For the collapse threshold we use the standard linearly extrapolated spherical-collapse value (Gunn and Gott 1972; Press and Schechter 1974).

$$\delta_{\rm c} = 1.686, \tag{24}$$

The peak-height parameter is therefore

$$\nu(M,z) = \frac{\delta_{\rm c}}{\sigma(M,z)} = \frac{\delta_{\rm c}}{D(z)\sigma(M,0)}. \tag{25}$$

Increasing halo mass reduces $\sigma(M,z)$, while increasing redshift reduces the linear growth factor. Both effects increase ν, so massive halos at high redshift correspond to increasingly rare peaks in the primordial density field.

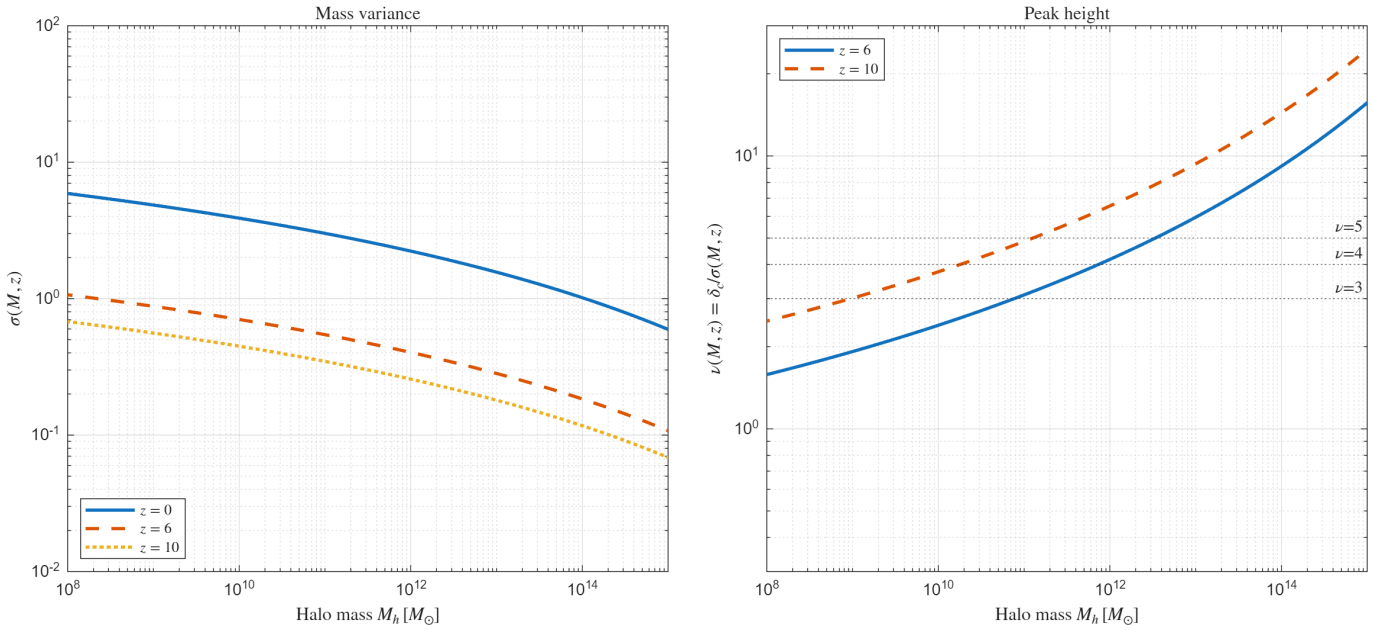


FIG. 1.— Mass variance $\sigma(M,z)$ and peak-height parameter $\nu(M,z)=\delta_c/\sigma(M,z)$ at representative redshifts. Increasing mass and redshift move halos toward the rare, high-ν tail of the density field.

2.5. *Press–Schechter and Sheth–Tormen Halo Mass Functions*

The HMF gives the comoving number density of collapsed dark-matter halos as a function of halo mass. We use the multiplicity-function convention

$$\frac{dn_X}{dM}(M,z)=\frac{\bar{\rho}_{\rm m}}{M^2}f_X(\nu)\times\left|\frac{d\ln\sigma^{-1}}{d\ln M}\right|. \tag{26}$$

The factor of ν is included explicitly in the multiplicity functions defined below. No additional factor of ν is therefore introduced through a separate $d\nu/dM$ term. The logarithmic form used for displaying the HMF is

$$\frac{dn_X}{d\log_{10}M}=(\ln 10)M\frac{dn_X}{dM}. \tag{27}$$

For Gaussian initial conditions and spherical collapse, the Press–Schechter multiplicity function is

$$f_{\rm PS}(\nu)=\sqrt{\frac{2}{\pi}}\,\nu\exp\left(-\frac{\nu^2}{2}\right) \tag{28}$$

(Press and Schechter 1974; Bond *et al.* 1991). Press–Schechter provides the basic analytic connection between the Gaussian density field and the abundance of collapsed objects.

The Sheth–Tormen prescription incorporates the effect of nonspherical, approximately ellipsoidal collapse and provides the principal HMF baseline used in this work (Sheth and Tormen 1999; Sheth *et al.* 2001). Its multiplicity function is

$$f_{\rm ST}(\nu)=A_{\rm ST}\sqrt{\frac{2a}{\pi}}\left[1+(a\nu^2)^{-p}\right]\times\nu\exp\left(-\frac{a\nu^2}{2}\right), \tag{29}$$

with

$$A_{\rm ST}=0.3222,\qquad a=0.707,\qquad p=0.3. \tag{30}$$

Relative to the spherical Press–Schechter result, ST predicts a different abundance in the rare high-mass tail that is particularly relevant to high-redshift galaxy and AGN applications. More generally, HMF calibrations depend on simulation methodology, halo finder, mass definition, cosmology, and redshift range (Tinker *et al.* 2008).

The cumulative number density of halos above a threshold $M_{\rm min}$ is

$$n_X(>M_{\rm min},z)=\int_{M_{\rm min}}^{\infty}\frac{dn_X}{dM'}(M',z)\,dM', \tag{31}$$

and the corresponding cumulative collapsed mass density is

$$\rho_{h,X}(>M_{\rm min},z)=\int_{M_{\rm min}}^{\infty}M'\frac{dn_X}{dM'}(M',z)\,dM'. \tag{32}$$

These two integral quantities play different roles in the applications below: n_X measures the number of potential hosts, whereas $\rho_{h,X}$ measures the total collapsed matter reservoir contained in those hosts.

2.6. *Bolshoi/Klypin-Calibrated Abundance Modification*

Analytic HMF prescriptions provide a useful theoretical description of halo collapse, but numerical simulations show that the abundance of halos can depart systematically from a single universal analytic form. Such differences become especially important when the objects of interest occupy the exponentially suppressed high-mass tail. To quantify the sensitivity of the present calculations to HMF calibration, we consider the Bolshoi/Klypin high-redshift abundance modification (Klypin *et al.* 2011).

The redshift-dependent correction factor is

$$F_{\rm K}(z)=\frac{[5.501D(z)]^4}{1+[5.500D(z)]^4}, \tag{33}$$

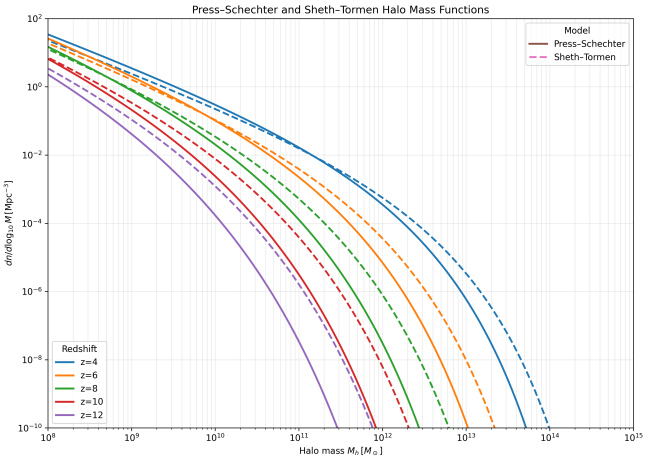


FIG. 2.— Press–Schechter and Sheth–Tormen halo mass functions at representative redshifts, calculated from the same normalized linear matter spectrum. The comparison illustrates the sensitivity of the rare-halo population to the adopted collapse prescription.

where $D(z)$ is the normalized growth factor defined in Equation (19). We define the Klypin-corrected Sheth–Tormen branch, denoted KST, by

$$\frac{dn_{\rm KST}}{dM}(M,z) = F_{\rm K}(z)\frac{dn_{\rm ST}}{dM}(M,z). \tag{34}$$

Since $F_{\rm K}(z)$ is independent of mass in this implementation, the correction factors out of cumulative integrals:

$$n_{\rm KST}(>M,z) = F_{\rm K}(z) n_{\rm ST}(>M,z), \tag{35}$$

and

$$\rho_{h,\rm KST}(>M,z) = F_{\rm K}(z)\rho_{h,\rm ST}(>M,z). \tag{36}$$

The ST and KST calculations therefore share the same background cosmology, linear power spectrum, growth factor, mass variance, collapse threshold, peak-height parameter, and halo-to-observable mappings. Their difference isolates the effect of the adopted abundance calibration.

For reference, the correction factors most directly relevant to the high-redshift comparisons are

$$\begin{aligned} F_{\rm K}(6) &\simeq 0.496, \\ F_{\rm K}(8) &\simeq 0.265, \\ F_{\rm K}(10) &\simeq 0.139. \end{aligned} \tag{37}$$

These correspond to progressively stronger reductions of the predicted halo supply toward cosmic dawn. The KST branch is used as a controlled simulation-motivated sensitivity test rather than as a unique or definitive replacement for the ST mass function.

2.6.1. *Halo-mass definition and calibration range*

A simulation-calibrated HMF must be interpreted together with its halo finder and halo-mass definition. Friends-of-friends masses, virial masses, and spherical-overdensity masses defined relative to either the critical density or the mean matter density are not generally interchangeable. This issue is particularly important in the rare high-mass tail, where modest shifts in halo mass can produce large changes in cumulative abundance.

In the analytic calculation used here, the halo-mass coordinate is associated with the spherical smoothing scale through

$$M_h = \frac{4\pi}{3}\bar{\rho}_{\rm m} R^3. \tag{38}$$

The same mass coordinate and numerical mass grid are used in the ST and KST branches. Equation (34) should therefore be understood as a controlled abundance modification within this common calculation, rather than as an exact transformation between different simulation halo-mass definitions. Precision comparisons with simulation catalogs or observationally inferred host masses require all quantities to be placed on a consistent mass definition.

The adopted Bolshoi/Klypin calibration is applied over

$$0 \le z \le 10. \tag{39}$$

Equation (33) can be evaluated mathematically at larger redshift, but values beyond this interval are extrapolations rather than simulation-calibrated predictions. High-redshift observational points beyond $z = 10$ can therefore provide useful context without being interpreted as calibrated KST constraints.

2.7. *Connection to the Observational Tests*

The quantities defined above provide the common cosmological halo supply for the three observational applications. Their relationship can be written schematically as

$$\begin{aligned} P_{\rm m}(k,z) &\longrightarrow \sigma(M,z) \longrightarrow \nu(M,z) \\ &\longrightarrow \frac{dn_X}{dM} \longrightarrow \{n_X(>M,z), \rho_{h,X}(>M,z)\}\,. \end{aligned} \tag{40}$$

The massive-galaxy test combines these quantities with the cosmic baryon fraction and a stellar-conversion efficiency to determine whether the available halo population can support the inferred stellar masses and number densities. The AGN test combines the cumulative host supply with black-hole occupation, activity, and host-mass assumptions. The UV luminosity-function test instead maps individual halo masses into stellar UV luminosities and propagates the differential HMF into an observable luminosity distribution.

This construction separates the cosmological and astrophysical components of each comparison. The HMF determines the number and mass reservoir of potential hosts. Baryonic conversion, black-hole occupation and duty cycle, and halo-to-light relations determine how that halo population is converted into observable galaxies and

AGN. The following sections use this common framework to test each observable population separately.

3. BARYONIC-RESERVOIR AND MASSIVE-GALAXY TEST

The first observational application of the halo-abundance framework is the massive-galaxy test. The central question is whether the dark-matter halo population at a given redshift provides both (i) a sufficiently large baryonic reservoir to support the inferred stellar masses and (ii) a sufficient number of such halos to reproduce the observed population. These are related but distinct requirements. The first is a mass-budget constraint set by the cosmic baryon fraction and the efficiency of converting baryons into stars; the second is an abundance constraint set by the halo mass function (HMF).

This distinction is especially important at high redshift. Massive halos correspond to increasingly rare peaks in the primordial density field, so a moderate increase in the halo mass required to host an observed galaxy can produce a large decrease in its predicted abundance. The massive-galaxy test therefore provides a direct way to connect the inferred properties of early JWST galaxies to the cosmological supply of collapsed halos, while keeping the baryonic assumptions explicit.

3.1. *From Halo Mass to the Available Baryonic Reservoir*

For the cosmological parameters adopted in this work, the cosmic baryon fraction is

$$f_b = \frac{\Omega_b}{\Omega_m} \simeq 0.156. \tag{41}$$

A halo of mass M_h therefore contains, at most, a cosmic-mean baryonic reservoir

$$M_b = f_b M_h. \tag{42}$$

If an effective fraction $\epsilon_\star$ of this reservoir is converted into stars, the stellar mass satisfies

$$M_\star \leq \epsilon_\star f_b M_h, \qquad 0 < \epsilon_\star \leq 1. \tag{43}$$

Consequently, an observed galaxy with inferred stellar mass $M_\star$ requires a minimum host-halo mass

$$M_{h,\min} = \frac{M_\star}{\epsilon_\star f_b}. \tag{44}$$

The limiting case $\epsilon_\star = 1$ corresponds to conversion of the entire cosmic-mean baryonic allotment into stars. It is therefore an absolute baryonic ceiling rather than a realistic star-formation efficiency. For $\epsilon_\star < 1$, a larger halo mass is required to support the same $M_\star$, moving the putative host farther into the rare high-mass tail of the HMF. This simple relation is useful because it separates the finite baryonic mass budget from the subsequent question of whether halos of the required mass exist in sufficient numbers (Behroozi *et al.* 2013; Moster *et al.* 2013; Boylan-Kolchin 2023).

For an HMF prescription $X \in \{\mathrm{ST}, \mathrm{KST}\}$, the cumulative halo abundance above the required threshold is

$$n_X(> M_{h,\min}, z) = \int_{M_{h,\min}}^{\infty} \frac{dn_X}{dM_h'}(M_h', z)\, dM_h'. \tag{45}$$

The corresponding massive-galaxy number-density test is therefore

$$n_{\mathrm{gal,obs}}(> M_\star, z) \quad \text{versus} \quad n_X\left(> \frac{M_\star}{\epsilon_\star f_b}, z\right). \tag{46}$$

An inferred stellar mass alone is thus not a cosmological abundance constraint: it becomes one only after specifying the stellar-to-halo mapping and comparing the resulting halo requirement with the observed galaxy number density.

3.2. *Differential Halo Supply*

Figure 3 compares the differential halo abundance predicted by the standard Sheth–Tormen (ST) mass function with the Bolshoi/Klypin-corrected ST (KST) prescription at representative redshifts. The ST calculation provides the principal analytic baseline. The KST branch uses the redshift-dependent correction $F_{\mathrm{K}}(z)$ defined in Section 2.6, so that

$$\frac{dn_{\mathrm{KST}}}{dM_h} = F_{\mathrm{K}}(z)\frac{dn_{\mathrm{ST}}}{dM_h}. \tag{47}$$

Because the adopted correction is independent of halo mass at fixed redshift, it changes the abundance normalization while preserving the mass dependence of the implemented ST curve. The underlying matter power spectrum, growth factor, mass variance, and peak-height parameter are identical in the two branches.

The comparison illustrates the increasing sensitivity of the available halo population to HMF calibration toward cosmic dawn. At low redshift the ST and KST predictions are close, whereas their separation becomes progressively larger at high redshift. For the massive-galaxy test this means that the same stellar-mass requirement and the same baryonic conversion efficiency can correspond to substantially different predicted host abundances depending on the adopted HMF calibration.

3.3. *Boylan–Kolchin/Labbé Number-Density Stress Test*

The cumulative abundance of halos above a mass threshold M_h is

$$n_X(> M_h, z) = \int_{M_h}^{\infty} \frac{dn_X}{dM'}(M', z)\, dM', \qquad X \in \{\mathrm{ST}, \mathrm{KST}\}. \tag{48}$$

Combining this quantity with Equation (44) maps an inferred stellar mass into the abundance of halos capable of hosting such a galaxy.

Figure 4 presents this comparison in the redshift–stellar-mass plane. At a fixed cumulative number density, the HMF sets the corresponding halo-mass threshold, and the baryonic relation converts that threshold into the maximum stellar mass supportable for an assumed $\epsilon_\star$. Since the KST abundance is lower than the ST abundance at a fixed halo mass and redshift, a given cumulative number density is reached at a lower halo-mass threshold in KST. The maximum stellar mass supportable at that number density is therefore also reduced.

Representative Boylan–Kolchin/Labbé stress-test systems near $z \simeq 7.5$ and $z \simeq 9.1$ illustrate the region in which the required host halos are already rare (Labb

'e *et al.* 2023; Boylan-Kolchin 2023). The $\epsilon_\star = 1$ curves provide the most permissive possible baryonic interpretation. Any smaller conversion efficiency increases the

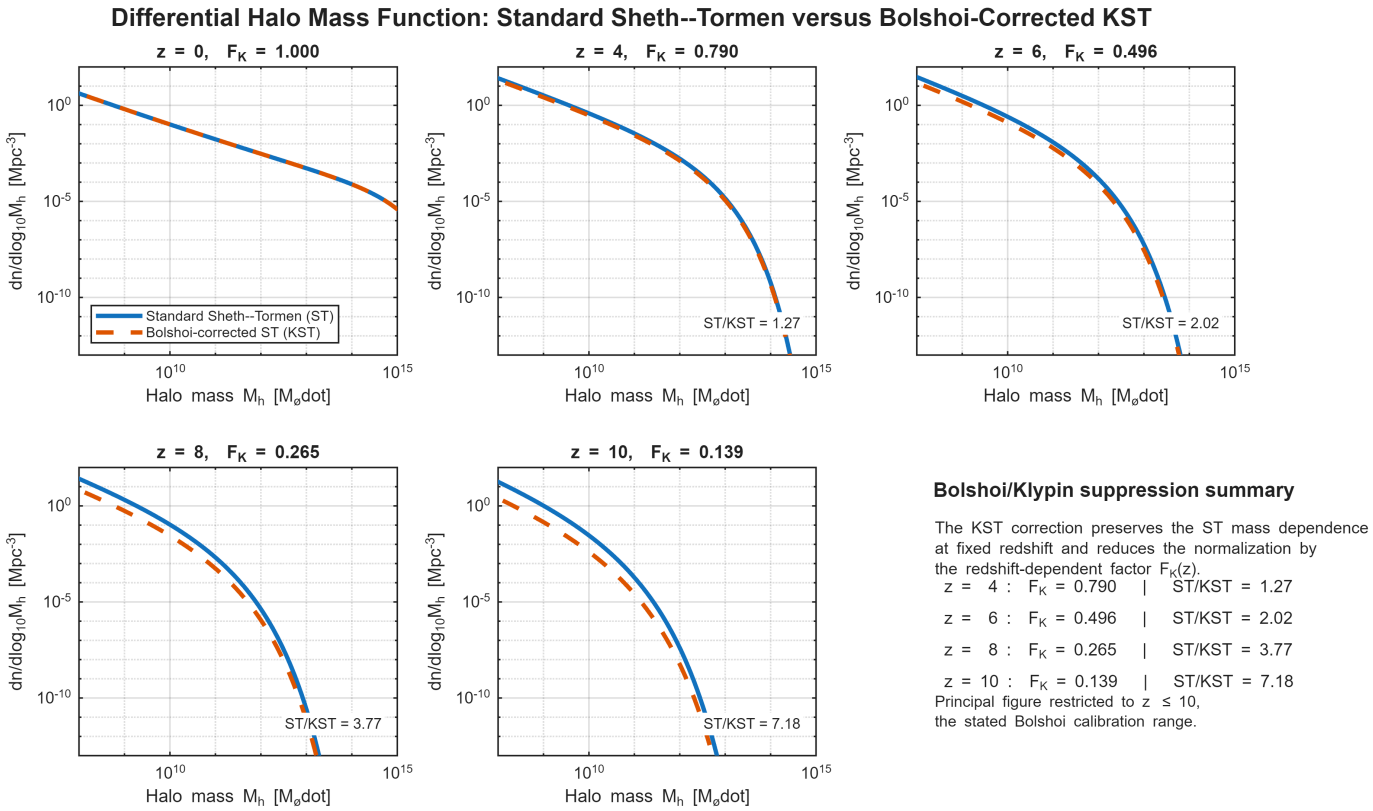


FIG. 3.— Differential halo mass function comparing the standard Sheth–Tormen (ST) prediction with the Bolshoi/Klypin-corrected ST (KST) prescription at $z = 0$, 4, 6, 8, and 10. At fixed redshift the KST correction rescales the ST abundance by $F_{\rm K}(z)$ while preserving the mass dependence of the implemented ST curve. The separation grows toward high redshift as the available population of massive halos becomes increasingly sensitive to the adopted HMF calibration. The calibrated KST comparison is restricted to $z \leq 10$.

required host-halo mass and makes the abundance constraint correspondingly stronger.

The comparison should not be interpreted as a model-independent exclusion of ΛCDM. Its significance depends jointly on the inferred stellar mass, redshift, survey volume, completeness, cosmic variance, lensing where applicable, and the assumed stellar-conversion efficiency. Because the high-mass HMF is steep, comparatively modest changes in the inferred host mass can produce large changes in the predicted abundance. The calculation is therefore most appropriately interpreted as a stress test of the combined halo-supply and baryonic mapping.

3.4. *Peak Height and the Rarity of Massive Hosts*

A complementary description of the massive-galaxy problem is provided by the peak-height parameter

$$\nu(M_h, z) = \frac{\delta_c}{\sigma(M_h, z)}, \tag{49}$$

where $\delta_c \simeq 1.686$. At fixed halo mass, $\sigma(M_h, z)$ decreases toward high redshift and ν therefore increases. Massive halos at cosmic dawn consequently correspond to increasingly rare fluctuations in the primordial density field.

Figure 5 shows fixed-ν tracks together with the baryonic relation $M_b = f_b M_h$. The diagram provides a direct physical view of how the stellar masses associated with the most massive early galaxies map onto increasingly rare host halos. The peak-height relation is determined by the linear density field, whereas the HMF calibration determines the abundance assigned to the resulting halo population. The two quantities therefore provide complementary information: ν characterizes the rarity of the underlying fluctuation, while dn/dM_h determines the number of collapsed halos available to host the observed systems.

3.5. *Cumulative Matter and Stellar-Mass-Density Constraints*

The number-density test considers whether enough individual halos exist above a specified mass threshold. A complementary integral constraint follows from the total collapsed matter contained in those halos. The cumulative halo-mass density is

$$\rho_{h,X}(>M_h, z) = \int_{M_h}^{\infty} M' \frac{dn_X}{dM'}(M', z)\, dM', \qquad X \in \{\mathrm{ST}, \mathrm{KST}\}. \tag{50}$$

For the adopted mass-independent KST prescription,

$$\rho_{h,\mathrm{KST}}(>M_h, z) = F_{\rm K}(z)\, \rho_{h,\mathrm{ST}}(>M_h, z). \tag{51}$$

The maximum stellar-mass density associated with galaxies above a stellar-mass threshold $M_\star$ is then

$$\rho_{\star,\max,X}(>M_\star, z) = \epsilon_\star f_b\, \rho_{h,X}\left(>\frac{M_\star}{\epsilon_\star f_b}, z\right), \qquad X \in \{\mathrm{ST}, \mathrm{KST}\}. \tag{52}$$

Figure 6 applies this integral constraint at representative high redshifts. The halo-mass reservoir is converted

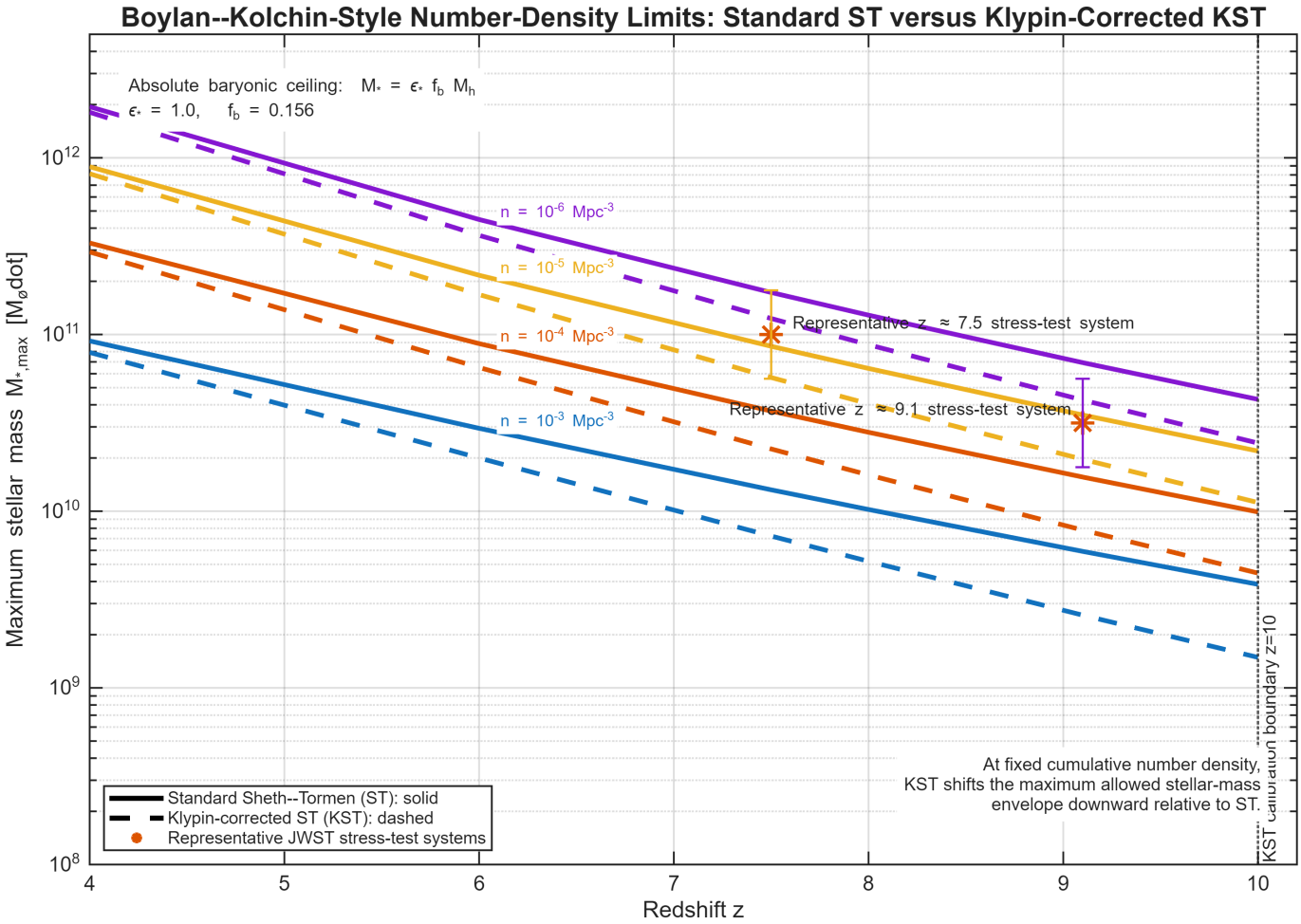


FIG. 4.— Boylan–Kolchin-style number-density stress test comparing the standard ST and KST halo reservoirs. Curves show the maximum stellar mass supportable at fixed cumulative halo number density under $M_\star = \epsilon_\star f_b M_h$, with $\epsilon_\star = 1$ representing the absolute baryon-conversion ceiling. Representative systems near $z \simeq 7.5$ and $z \simeq 9.1$ are shown with their observational uncertainty ranges. The lower KST halo abundance makes a fixed stellar-mass/number-density combination more demanding. The $z = 10$ marker denotes the upper boundary of the adopted KST calibration.

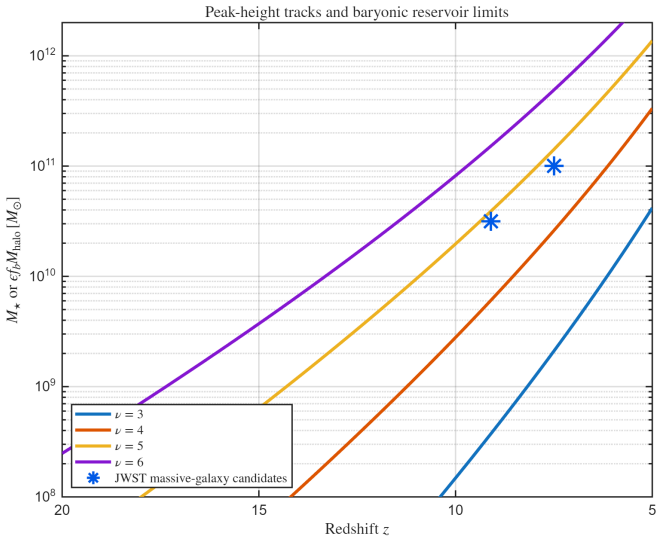


FIG. 5.— Peak-height tracks and baryonic-reservoir limits. Curves of fixed ν identify halo masses corresponding to increasingly rare primordial density peaks. At high redshift, massive galaxy hosts occupy progressively rarer high-ν regions. The baryonic relation $M_b = f_b M_h$ converts the halo-mass scale into the corresponding maximum cosmic-mean baryonic reservoir.

into a maximum stellar-mass density using the same baryonic prescription for both HMF branches. The $\epsilon_\star = 1$ sequence again represents an absolute baryonic ceiling: an observed stellar-mass density above this limit cannot be accommodated under the simultaneous assumptions entering the calculation. A measurement below but close to the ceiling is less decisive, because modest changes in stellar mass, redshift, completeness, survey volume, or the stellar-to-halo mapping can shift the comparison appreciably.

The Boylan–Kolchin/Labbé benchmark provides a direct observational comparison with the calculated mass reservoir. The KST abundance reduction propagates into the integrated halo-mass density before any baryonic conversion efficiency is applied. Consequently, its stellar-mass-density ceiling lies below the corresponding ST prediction. This result emphasizes that an assessment of very massive high-redshift galaxies depends not only on the available cosmic baryon fraction but also on the abundance calibration of the rare host halos in which those baryons reside.

3.6. *Interpretation of the Massive-Galaxy Test*

The massive-galaxy calculation can be summarized by the sequence

$$\begin{aligned} M_\star &\longrightarrow M_{h,\min} = \frac{M_\star}{\epsilon_\star f_b} \\ &\longrightarrow \{n_X(>M_{h,\min}, z),\ \rho_{h,X}(>M_{h,\min}, z)\} \\ &\longrightarrow \text{massive-galaxy consistency test.} \end{aligned} \tag{53}$$

The first step is controlled by the baryonic mapping; the second is controlled by the cosmological halo population. Treating these ingredients separately makes clear why neither a large inferred stellar mass nor a low predicted halo abundance is sufficient by itself to establish a cosmological inconsistency.

The calculations show that massive high-redshift galaxies are particularly sensitive probes because their required hosts can lie on the exponentially suppressed rare-halo tail. In this regime the inferred degree of tension depends jointly on the stellar-to-halo conversion efficiency and the adopted HMF calibration. Standard ST provides a comparatively larger high-redshift halo reservoir, whereas the illustrative KST calibration lowers both the cumulative number of suitable halos and the integrated collapsed mass available to support their stellar populations.

These results are therefore best interpreted as quantitative stress tests of the combined cosmological and baryonic model rather than as binary falsification criteria. A robust claim of inconsistency would require the discrepancy to persist across physically plausible uncertainties in stellar population modeling, stellar mass, redshift, lensing magnification, completeness, survey volume, cosmic variance, halo-mass definition, and baryonic conversion efficiency (Boylan-Kolchin 2023). Within the controlled comparison developed here, the background cosmology and baryonic mapping are held fixed between ST and KST, so their difference isolates the sensitivity of the massive-galaxy constraint to the adopted halo-abundance calibration.

The next application considers active galactic nuclei, for which the same cosmological halo supply must be supplemented by black-hole occupation, duty cycle, accretion physics, and the relation between black-hole properties and host-halo mass.

4. AGN HOST-ABUNDANCE TEST

The second application of the halo-abundance framework concerns active galactic nuclei (AGN) at high redshift. The cosmological part of the problem is set by the number of dark-matter halos available to host the observed population. The astrophysical part is more complex than for the massive-galaxy test because an eligible halo need not contain a black hole of the required mass, and a black hole that is present need not be observed in an active accretion phase. The predicted AGN abundance therefore depends on the minimum host-halo mass, black-hole occupation fraction, AGN duty cycle, and the mapping between AGN luminosity, black-hole mass, and halo mass.

The purpose of the calculation is to keep these ingredients explicit. The HMF determines the cosmological supply of potential hosts, while the occupation and activity factors determine what fraction of those hosts can appear in a selected AGN sample. This provides a direct way to identify combinations of host mass and AGN astrophysics that become increasingly demanding at early cosmic times.

4.1. *AGN Halo Occupation*

For a halo of mass M_h at redshift z, the mean number of observable AGN may be written

$$\begin{aligned} \langle N_{\rm AGN} \mid M_h, z\rangle = f_{\rm occ}(M_h, z)\, f_{\rm duty}(M_h, z) \\ \times \langle N_{\rm BH,eligible} \mid M_h, z\rangle\,, \end{aligned} \tag{54}$$

where $f_{\rm occ}$ is the fraction of eligible halos containing a black hole capable of participating in the selected population, $f_{\rm duty}$ is the fraction of those systems observed in the relevant active state, and $\langle N_{\rm BH,eligible} \mid M_h, z\rangle$ is the mean number of black holes satisfying the adopted eligibility conditions.

For the rare high-redshift systems considered here, a transparent limiting model is the one-central-black-hole approximation,

$$\langle N_{\rm BH,eligible} \mid M_h, z\rangle \simeq \Theta(M_h - M_{\rm min}), \tag{55}$$

where Θ is the Heaviside step function and $M_{\rm min}$ is the minimum host-halo mass associated with the selected AGN population. This approximation treats the abundance test in terms of one relevant central black hole per eligible halo.

The corresponding AGN number density for HMF prescription X is

$$\begin{aligned} n_{{\rm AGN},X}(z) = \int_{M_{\rm min}}^{\infty} f_{\rm occ}(M_h, z) f_{\rm duty}(M_h, z) \\ \times \frac{dn_X}{dM_h}(M_h, z)\, dM_h, \end{aligned} \tag{56}$$

with $X \in \{\mathrm{ST}, \mathrm{KST}\}$. If $f_{\rm occ}$ and $f_{\rm duty}$ are approximated as constants above $M_{\rm min}$, this becomes

$$n_{{\rm AGN},X}(z) = f_{\rm occ} f_{\rm duty}\, n_X(>M_{\rm min}, z). \tag{57}$$

Equation (57) separates the cosmological and astrophysical factors particularly clearly. The cumulative HMF

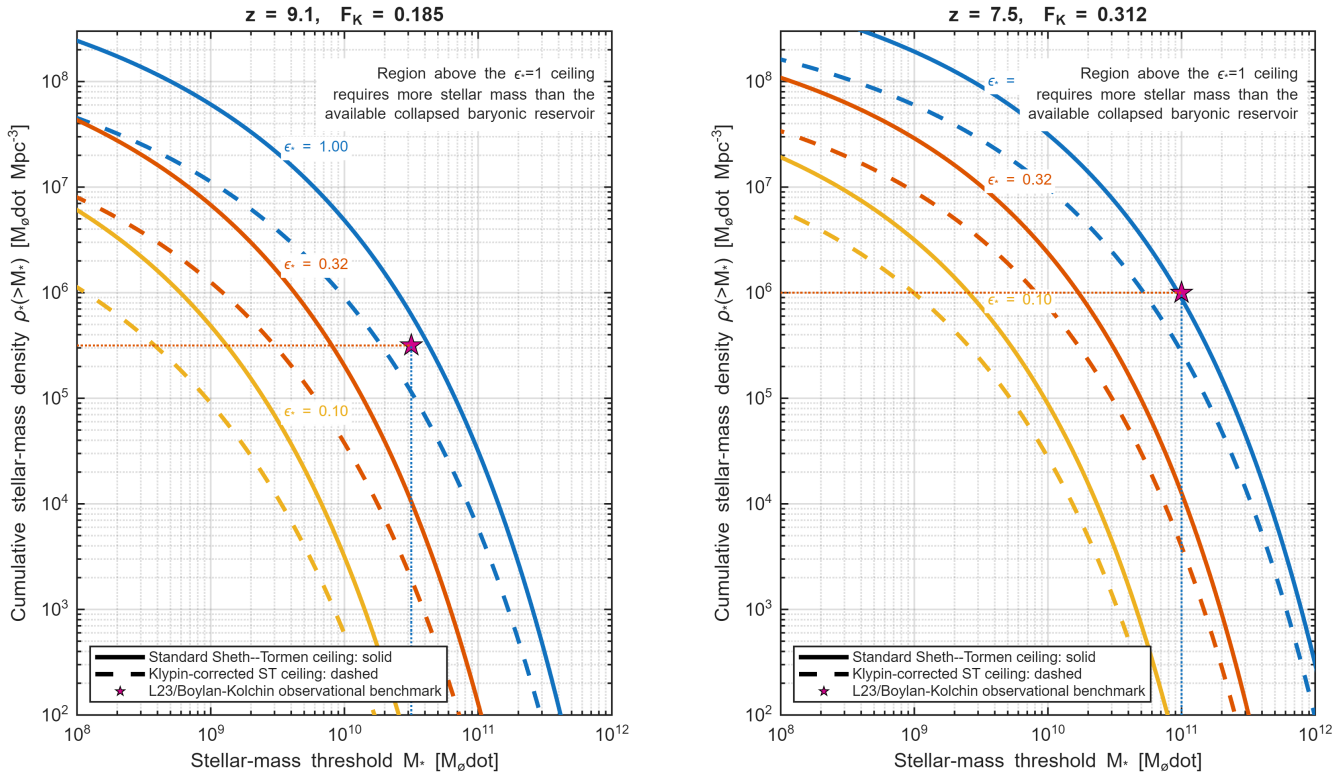


FIG. 6.— Cumulative matter-density and maximum stellar-mass-density constraints comparing standard ST and KST predictions at representative high redshifts. The halo-mass reservoir is converted into stellar-mass-density ceilings using the same baryonic mapping for both HMF branches. The $\epsilon_\star = 1$ sequence gives the absolute baryon-conversion ceiling, while lower efficiencies require more massive and rarer host halos. The Boylan–Kolchin/Labbé benchmark illustrates the observational massive-galaxy stress test.

specifies the number of potential hosts, while $f_{\rm occ} f_{\rm duty}$ specifies the fraction that appear in the selected active population. Since both factors are bounded above by unity,

$$0 \le f_{\rm occ} \le 1, \qquad 0 \le f_{\rm duty} \le 1, \tag{58}$$

the cumulative halo abundance provides an absolute host-supply ceiling for a specified $M_{\rm min}$.

The occupation fraction and duty cycle represent different physics. Black-hole occupation depends on seeding, retention, mergers, and subsequent black-hole growth, whereas the duty cycle describes the episodic nature of accretion and depends on gas supply, angular-momentum transport, feedback, environment, and the luminosity threshold defining the sample (Volonteri 2010; Inayoshi *et al.* 2020). They should therefore not be interpreted as interchangeable parameters.

4.2. *AGN Duty Cycle and the Host-Supply Ceiling*

In a simple time-domain interpretation, the duty cycle may be written

$$f_{\rm duty} = \frac{t_{\rm active}}{t_{\rm available}}, \tag{59}$$

where $t_{\rm active}$ is the time spent above the adopted activity or luminosity threshold and $t_{\rm available}$ is the relevant comparison interval. The precise interpretation is sample dependent: the available interval may correspond to a redshift-bin duration, a black-hole growth interval, or another physically motivated timescale.

The limiting choice

$$f_{\rm duty} = 1 \tag{60}$$

assumes that every occupied and otherwise eligible system is observed in the selected active state. For a fixed host population this maximizes the predicted AGN abundance and therefore provides the least restrictive halo-supply bound. If an observed abundance is difficult to accommodate even under $f_{\rm occ} = f_{\rm duty} = 1$, reducing either factor cannot alleviate that particular host-supply constraint.

Conversely, the duty cycle cannot be interpreted independently of $M_{\rm min}$. The cumulative halo abundance can change extremely rapidly with host mass in the rare-halo regime. A moderate reduction in the inferred minimum host mass can therefore increase the available halo population by a large factor, while a smaller duty cycle reduces the fraction of that population observed as AGN. The two effects must be considered jointly.

For the ST and KST branches, identical occupation, duty-cycle, and host-mass assumptions give

$$n_{\rm AGN,KST}(z) = F_{\rm K}(z)\, n_{\rm AGN,ST}(z). \tag{61}$$

Thus the HMF calibration changes the cosmological supply of eligible hosts but does not prescribe a different AGN lifetime, black-hole seeding efficiency, or accretion history.

4.3. *AGN Halo-Supply Constraints*

Figure 7 shows the maximum AGN abundance permitted by the halo population as a function of redshift,

compared directly with the high-redshift AGN abundance data of Dayal *et al.* (2025) plotted in the figure. The left panel illustrates the strong dependence on minimum host-halo mass under the maximally permissive $f_{\rm occ} = f_{\rm duty} = 1$ assumption. If the selected AGN can occupy halos with $M_h \sim 10^{11}\,M_\odot$, the potential host population is much larger than if halos of 10^{12}–$10^{13}\,M_\odot$ are required. The latter rapidly enter the rare-halo tail toward high redshift.

The right panel shows the additional suppression associated with the duty cycle for a representative host threshold. For an observed AGN number density $n_{\rm AGN,obs}$, Equation (57) implies the necessary condition

$$f_{\rm duty} f_{\rm occ} \geq \frac{n_{\rm AGN,obs}}{n_X(>M_{\rm min}, z)}. \tag{62}$$

Since $f_{\rm duty} f_{\rm occ} \leq 1$, a specified host threshold cannot supply the observed population within HMF branch X if

$$n_{\rm AGN,obs} > n_X(>M_{\rm min}, z). \tag{63}$$

Representative JWST high-redshift black-hole and AGN abundance estimates are shown as observational benchmarks. These points should not be interpreted as direct measurements of host-halo mass. Their conversion into a halo constraint depends on black-hole masses, bolometric corrections, Eddington ratios, AGN classification, selection functions, survey volume, completeness, and the black-hole–halo relation. The comparison instead asks whether a specified set of host and activity assumptions provides a sufficiently large cosmological reservoir of candidate halos.

4.4. *From AGN Luminosity to Black-Hole Mass*

The halo abundance cannot be compared with a luminosity-selected AGN sample until the observed luminosity is related to a characteristic black-hole and host-halo mass. For a black hole of mass $M_{\rm BH}$, the Eddington luminosity is

$$L_{\rm Edd} = \frac{4\pi G M_{\rm BH} m_p c}{\sigma_{\rm T}}, \tag{64}$$

where m_p is the proton mass and $\sigma_{\rm T}$ is the Thomson cross section. Numerically,

$$L_{\rm Edd} \simeq 1.26 \times 10^{38} \left(\frac{M_{\rm BH}}{M_\odot}\right) {\rm erg\,s^{-1}}. \tag{65}$$

Defining the Eddington ratio

$$\lambda_{\rm Edd} = \frac{L_{\rm bol}}{L_{\rm Edd}}, \tag{66}$$

the bolometric luminosity is

$$L_{\rm bol} = \lambda_{\rm Edd} L_{\rm Edd}. \tag{67}$$

A luminosity threshold $L_{\rm min}$ therefore corresponds to a minimum black-hole mass

$$M_{\rm BH,min} = \frac{L_{\rm min}\sigma_{\rm T}}{4\pi G m_p c\,\lambda_{\rm Edd}}. \tag{68}$$

This relation illustrates an important degeneracy. At fixed luminosity, a smaller Eddington ratio requires a more massive black hole, whereas a source radiating closer to the Eddington limit can produce the same luminosity with a smaller $M_{\rm BH}$. A luminosity-selected sample therefore does not define a unique black-hole mass unless the Eddington-ratio distribution is specified.

4.5. *From Black-Hole Mass to Host-Halo Mass*

A second relation is required to map black-hole mass into host-halo mass. For a transparent phenomenological parameterization, define

$$\epsilon_{\rm BH} = \frac{M_{\rm BH}}{M_h}, \tag{69}$$

so that

$$M_{\rm BH} = \epsilon_{\rm BH} M_h. \tag{70}$$

Here $\epsilon_{\rm BH}$ is an effective black-hole-to-halo mass ratio. It is not a radiative efficiency and is not assumed to be a universal constant. Observed correlations between black-hole mass and host properties provide physical motivation for such a mapping, but their form, scatter, and redshift evolution remain important uncertainties (Kormendy and Ho 2013; Volonteri 2010; Inayoshi *et al.* 2020).

Combining Equations (68) and (70) gives the characteristic minimum host mass

$$M_{\rm min} = \frac{M_{\rm BH,min}}{\epsilon_{\rm BH}}, \tag{71}$$

or, explicitly,

$$M_{\rm min} = \frac{L_{\rm min}\sigma_{\rm T}}{4\pi G m_p c} \times \frac{1}{\lambda_{\rm Edd}\epsilon_{\rm BH}}. \tag{72}$$

Equation (72) makes explicit that the required host mass varies inversely with both the assumed Eddington ratio and the effective black-hole-to-halo mass ratio.

Figure 8 illustrates this mapping. A luminous AGN can be associated with a larger black hole, a larger Eddington ratio, a larger black-hole-to-halo mass ratio, or some combination of these quantities. Consequently, luminosity alone does not uniquely determine $M_{\rm min}$. Once a mapping is specified, however, the cumulative HMF supplies a direct abundance test of the required hosts.

4.6. *Clustering as an Independent Host-Mass Test*

AGN clustering provides a complementary way to test the host masses inferred from abundance arguments. Massive halos correspond to rarer peaks and generally have larger large-scale bias. An AGN population assigned to very massive halos should therefore exhibit stronger clustering than one occupying more common, lower-mass halos (Bardeen *et al.* 1986; Sheth *et al.* 2001).

For HMF prescription X, the effective AGN bias can be written

$$b_{{\rm AGN},X}(z) = \frac{\displaystyle\int_0^\infty b_h(M_h,z)\,\langle N_{\rm AGN} \mid M_h, z\rangle\,\frac{dn_X}{dM_h}\,dM_h}{\displaystyle\int_0^\infty \langle N_{\rm AGN} \mid M_h, z\rangle\,\frac{dn_X}{dM_h}\,dM_h}, \tag{73}$$

where $b_h(M_h, z)$ is the linear halo bias. For the threshold model with mass-independent $f_{\rm occ}$ and $f_{\rm duty}$ above $M_{\rm min}$,

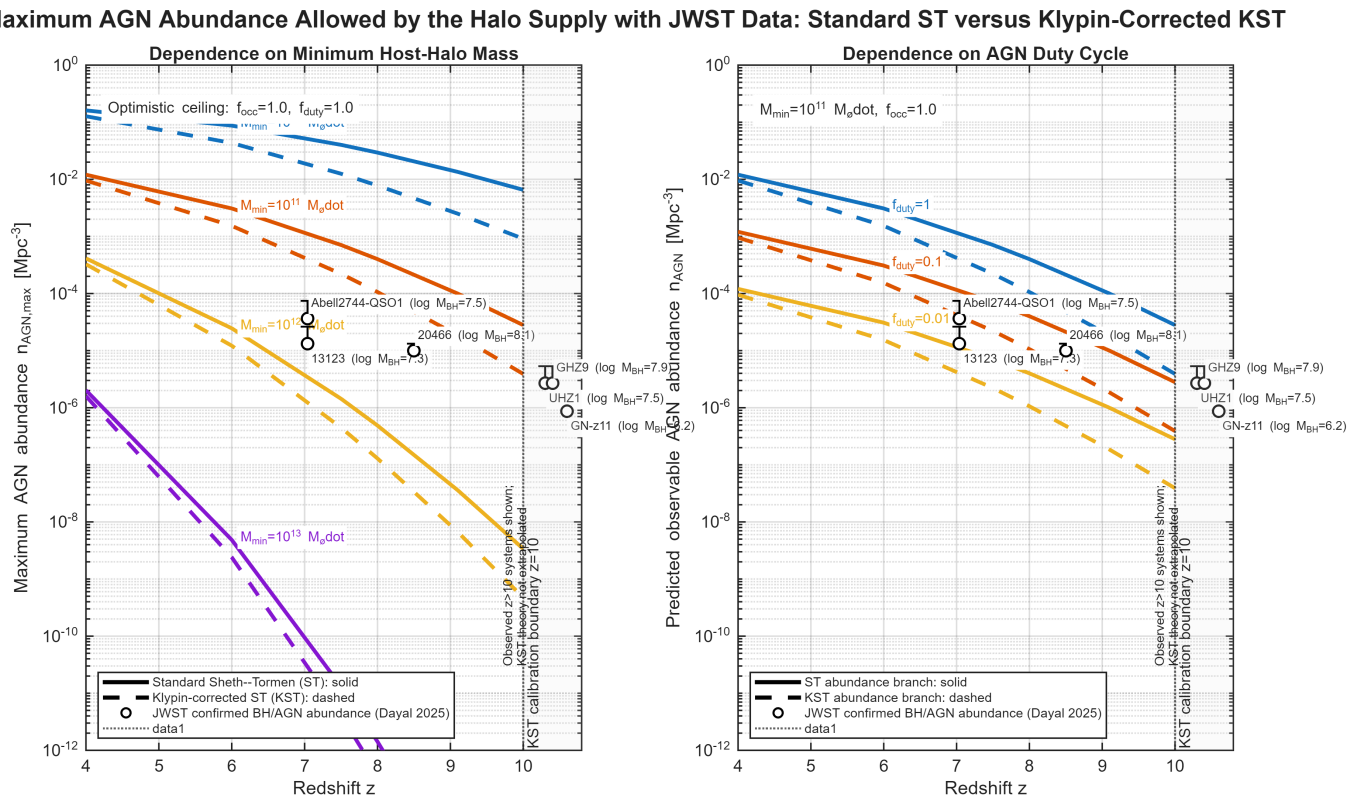


FIG. 7.— Maximum AGN abundance permitted by the available halo population as a function of redshift. The curves show the cumulative abundance of halos above the adopted minimum host-halo mass for the ST and KST halo mass functions, thereby providing an upper limit on the abundance of AGN that can be hosted by the corresponding halo population. The theoretical halo-supply limits are compared with the high-redshift AGN abundance constraints of Dayal *et al.* (2025), based on the emerging JWST population of faint and obscured AGN. The comparison illustrates whether the observed AGN abundance can be accommodated by the available host-halo population before introducing additional reductions associated with AGN occupation fractions or duty cycles.

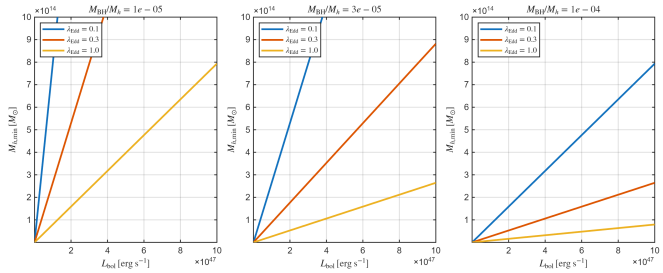


FIG. 8.— Mapping between AGN luminosity, black-hole mass, and characteristic host-halo mass. The Eddington ratio $\lambda_{\rm Edd}$ converts luminosity into black-hole mass, while the effective ratio $\epsilon_{\rm BH} = M_{\rm BH}/M_h$ maps black-hole mass into a host requirement. Different combinations of these parameters can therefore correspond to the same observed AGN luminosity.

these constant factors cancel:

$$b_{\rm AGN,}{}_X(z) = \frac{\displaystyle\int_{M_{\rm min}}^{\infty} b_h(M_h, z)\frac{dn_X}{dM_h}\,dM_h}{\displaystyle\int_{M_{\rm min}}^{\infty} \frac{dn_X}{dM_h}\,dM_h}. \qquad (74)$$

The abundance and clustering observables consequently constrain different aspects of the AGN–halo connection. The abundance measures how many eligible hosts exist, whereas the bias measures the characteristic rarity of those hosts. Increasing $M_{\rm min}$ lowers the available host abundance while generally increasing the predicted bias. A clustering measurement can therefore test whether the characteristic halo masses required by an abundance model are plausible.

For the particular KST prescription used here, the factor $F_{\rm K}(z)$ is independent of halo mass at fixed redshift. If the same halo-bias relation and the same occupation model are applied to both HMF branches, this common factor cancels between the numerator and denominator of Equation (73). Under these assumptions,

$$b_{\rm AGN,KST}(z) = b_{\rm AGN,ST}(z). \qquad (75)$$

Thus the KST modification changes the predicted AGN abundance but does not by itself generate a different normalized clustering bias. A difference in clustering would require a mass-dependent HMF modification, a different halo-bias calibration, or a change in the inferred occupation or host-mass distribution.

4.7. *Interpretation of the AGN Abundance Test*

The AGN calculation can be summarized by two coupled mappings. The first connects an observed AGN property to a characteristic host requirement,

$$L_{\rm bol} \longrightarrow M_{\rm BH} \longrightarrow M_{\rm min}, \tag{76}$$

where the conversion depends principally on $\lambda_{\rm Edd}$ and $\epsilon_{\rm BH}$. The second maps the host requirement into an observable population,

$$\begin{aligned} M_{\rm min} &\longrightarrow n_X(>M_{\rm min}, z) \\ &\longrightarrow f_{\rm occ} f_{\rm duty}\, n_X(>M_{\rm min}, z) \\ &\longrightarrow n_{{\rm AGN},X}(z). \end{aligned} \tag{77}$$

These relations make clear why an observed AGN abundance does not uniquely determine a host-halo mass. A low number density may reflect rare massive hosts, a small black-hole occupation fraction, a short duty cycle, or a combination of these effects. Conversely, explaining a comparatively large AGN abundance with very massive hosts can require occupation and duty-cycle factors approaching their physical upper limits.

The high-redshift comparison is therefore a conditional halo-supply test. A deficit of predicted AGN relative to an observed abundance can arise from the adopted HMF, the inferred minimum host mass, black-hole occupation, duty cycle, the black-hole–halo relation, the Eddington-ratio distribution, or observational selection. The HMF constrains the cosmological reservoir, but does not by itself provide a complete AGN luminosity function.

The quantitative KST abundance comparison is restricted to the calibration interval $z \leq 10$ defined in Section 2.6.1. Sources at higher redshift remain valuable for testing the luminosity–black-hole–halo mapping, but KST abundance estimates there are extrapolative. Within the calibrated interval, comparing ST and KST with identical occupation and activity assumptions isolates the sensitivity of the AGN host-supply constraint to the adopted halo-abundance calibration.

A more complete forward model would replace the single host threshold and constant occupation factors with distributions of black-hole mass, Eddington ratio, obscuration, variability, host-halo mass, and survey selection. The present framework provides the analytic baseline for such an extension by showing explicitly where each of these ingredients enters the abundance calculation.

The next section considers the third observational application: the high-redshift galaxy UV luminosity function. In that calculation the HMF is mapped into luminosity space through stellar and baryonic physics rather than through the AGN occupation and duty-cycle factors defined here.

5. HIGH-REDSHIFT UV LUMINOSITY-FUNCTION TEST

The third observational application connects the cosmological halo population to the rest-frame ultraviolet (UV) luminosities measured for galaxies at cosmic dawn. The halo mass function determines the abundance of collapsed dark-matter structures, whereas observations measure the radiation emitted by the baryonic component. A comparison between the two therefore requires two separate ingredients: a mapping from halo mass to UV luminosity and a calculation of the abundance of halos that populate each luminosity interval.

For a halo of mass M_h, the first ingredient may be written schematically as

$$M_h \longrightarrow M_{\rm UV}(M_h, z), \tag{78}$$

whereas the second is supplied by the differential HMF,

$$\frac{dn_X}{dM_h}(M_h, z), \qquad X \in \{{\rm ST}, {\rm KST}\}. \tag{79}$$

Combining these quantities produces the theoretical UV luminosity function $\Phi_X(M_{\rm UV}, z)$ that can be compared directly with observed galaxy number densities.

The distinction between luminosity and abundance is central to the interpretation. A baryonic model may allow a halo of a particular mass to produce a luminous galaxy, but population consistency additionally requires that halos of the required mass exist in sufficient numbers. Conversely, an adequate halo supply does not guarantee agreement with observations if the adopted baryonic prescription produces galaxies that are systematically too faint. The calculation below therefore keeps the halo-to-light physics and the cosmological abundance calculation explicit.

The observational motivation follows the rapidly developing JWST view of cosmic dawn, including massive galaxies, luminous UV sources, and candidate AGN at high redshift (Labb

'e *et al.* 2023; Boylan-Kolchin 2023; Harikane *et al.* 2023; Atek *et al.* 2023a,b; Maiolino *et al.* 2024; Franco *et al.* 2025; Donnan *et al.* 2023, 2024). The model is intended as a controlled first-order description of the connection between halo supply, baryonic conversion efficiency, and UV luminosity.

5.1. *Baryonic Conversion and Stellar Mass*

For a halo of mass M_h, the baryonic mass associated with the cosmic mean baryon fraction is

$$M_b = f_b M_h, \tag{80}$$

where

$$f_b = \frac{\Omega_b}{\Omega_m} \simeq 0.156. \tag{81}$$

The stellar mass is parameterized as

$$M_\star = \epsilon_\star f_b M_h, \tag{82}$$

where $\epsilon_\star$ is an effective integrated baryon-to-star conversion efficiency. The numerical calculations consider

$$\epsilon_\star = 0.03,\ 0.10,\ 0.20, \tag{83}$$

representing illustrative low, intermediate, and relatively high conversion efficiencies (Behroozi *et al.* 2013; Moster *et al.* 2013).

These values are not intended to define a universal efficiency law. In general, $\epsilon_\star$ may depend on halo mass, redshift, assembly history, feedback, and environment. Here it serves as a transparent parameter for examining how uncertainty in baryonic conversion propagates into the halo-to-UV mapping.

5.2. *Star-Formation Rate and Rest-Frame UV Luminosity*

The stellar mass is converted into a characteristic star-formation rate using the timescale

$$t_\star(z) = 0.1 H^{-1}(z). \tag{84}$$

The corresponding star-formation rate is

$$\mathrm{SFR}(M_h, z) = \frac{\epsilon_\star f_b M_h}{t_\star(z)}. \tag{85}$$

This prescription captures the approximate shortening of characteristic dynamical timescales toward high redshift without attempting to describe individual star-formation histories.

The rest-frame UV spectral luminosity is taken to be proportional to the star-formation rate,

$$L_{\nu,\mathrm{UV}} = \kappa_{\mathrm{UV}}\,\mathrm{SFR}, \tag{86}$$

with

$$\kappa_{\mathrm{UV}} = 8 \times 10^{27} \frac{\mathrm{erg\,s^{-1}\,Hz^{-1}}}{M_\odot\,\mathrm{yr^{-1}}}. \tag{87}$$

The UV conversion factor is an astrophysical calibration and may depend on the stellar initial mass function, metallicity, stellar population age, and star-formation history. It should therefore be regarded as part of the halo-to-light model rather than as a cosmological prediction (Bouwens *et al.* 2021; Finkelstein and Bagley 2022; Napolitano *et al.* 2025).

The corresponding AB absolute magnitude is

$$M_{\mathrm{UV}} = 51.60 - 2.5 \log_{10}\left(\frac{L_{\nu,\mathrm{UV}}}{\mathrm{erg\,s^{-1}\,Hz^{-1}}}\right). \tag{88}$$

Equations (85)–(88) define the deterministic mapping

$$M_{\mathrm{UV}} = M_{\mathrm{UV}}(M_h, z; \epsilon_\star). \tag{89}$$

At fixed redshift, increasing either M_h or $\epsilon_\star$ increases the UV luminosity and produces a more negative M_{UV}. At fixed halo mass and efficiency, redshift enters through $H(z)$ in the adopted star-formation timescale. The mapping itself is independent of the HMF prescription: ST and KST assign the same luminosity to a halo of specified M_h, z, and $\epsilon_\star$. Their distinction arises only when the abundance of such halos is evaluated.

5.3. *JWST Redshift–UV Luminosity Plane*

Figure 9 places representative high-redshift JWST galaxies and candidate AGN in the redshift–M_{UV} plane. Brighter sources have more negative UV absolute magnitudes. The observed population spans a regime in which luminous systems are already present at early cosmic times, motivating a direct connection between their measured UV luminosities and the halo masses capable of supporting them (Labb

'e *et al.* 2023; Boylan-Kolchin 2023; Harikane *et al.* 2023; Atek *et al.* 2023a,b; Maiolino *et al.* 2024).

The observational plane raises two related questions. First, what combinations of halo mass and baryonic conversion efficiency can produce the measured luminosities? Second, how abundant are halos satisfying those requirements at the corresponding redshifts? The first question is addressed by the halo-to-UV tracks below; the second requires transformation of the HMF into a UV luminosity function.

5.4. *Halo-to-UV Luminosity Tracks*

Figure 10 evaluates Equation (88) for representative halo masses

$$M_h = 10^{10},\, 10^{11},\, 10^{12},\, 10^{13}\,M_\odot \tag{90}$$

and the efficiencies in Equation (82). The resulting halo-to-UV luminosity tracks are compared with the spectroscopically confirmed high-redshift GLASS/NIRSpec sources of Napolitano *et al.* (2025) and with the massive-galaxy benchmarks reported by Labb

'e *et al.* (2023) (L23), whose implications for the available halo and baryonic reservoirs were examined by Boylan-Kolchin (2023). These comparisons place the simple halo-to-light mapping in direct observational context across the JWST redshift range. Increasing halo mass produces a brighter UV source, while increasing $\epsilon_\star$ allows a lower-mass halo to reach a comparable luminosity.

A measured M_{UV} therefore does not uniquely determine M_h. A luminous source may correspond to a comparatively massive halo with moderate conversion efficiency, a less massive halo undergoing unusually efficient or bursty star formation, or a UV continuum containing an AGN contribution. Stellar population age, metallicity, dust attenuation, and star-formation history introduce further uncertainty in the inversion from luminosity to halo mass.

The tracks thus define the conditional luminosity associated with a halo under the adopted baryonic model. The probability of observing such a system depends additionally on the abundance of halos at the corresponding mass and redshift.

5.5. *From the Halo Mass Function to the UV Luminosity Function*

The population-level prediction follows by combining the deterministic halo-to-light relation with the HMF. For a monotonic mapping, conservation of number gives

$$\Phi_X(M_{\mathrm{UV}}, z)\, dM_{\mathrm{UV}} = \frac{dn_X}{dM_h}(M_h, z)\, |dM_h|\,. \tag{91}$$

Hence,

$$\Phi_X(M_{\mathrm{UV}}, z) = \left.\frac{dn_X}{dM_h}(M_h, z) \left|\frac{dM_h}{dM_{\mathrm{UV}}}\right|\right|_{M_h = M_h(M_{\mathrm{UV}}, z)}, \tag{92}$$

where Φ_X has units of comoving number density per magnitude.

For the adopted linear luminosity scaling,

$$L_{\nu,\mathrm{UV}} \propto M_h, \tag{93}$$

and the magnitude relation can be written

$$M_{\mathrm{UV}} = C(z, \epsilon_\star) - 2.5 \log_{10} M_h, \tag{94}$$

where $C(z, \epsilon_\star)$ contains the baryon fraction, conversion efficiency, star-formation timescale, UV calibration, and unit normalization. It follows that

$$\frac{dM_{\mathrm{UV}}}{dM_h} = -\frac{2.5}{\ln 10}\frac{1}{M_h}, \tag{95}$$

and therefore

$$\left|\frac{dM_h}{dM_{\mathrm{UV}}}\right| = \frac{\ln 10}{2.5} M_h. \tag{96}$$

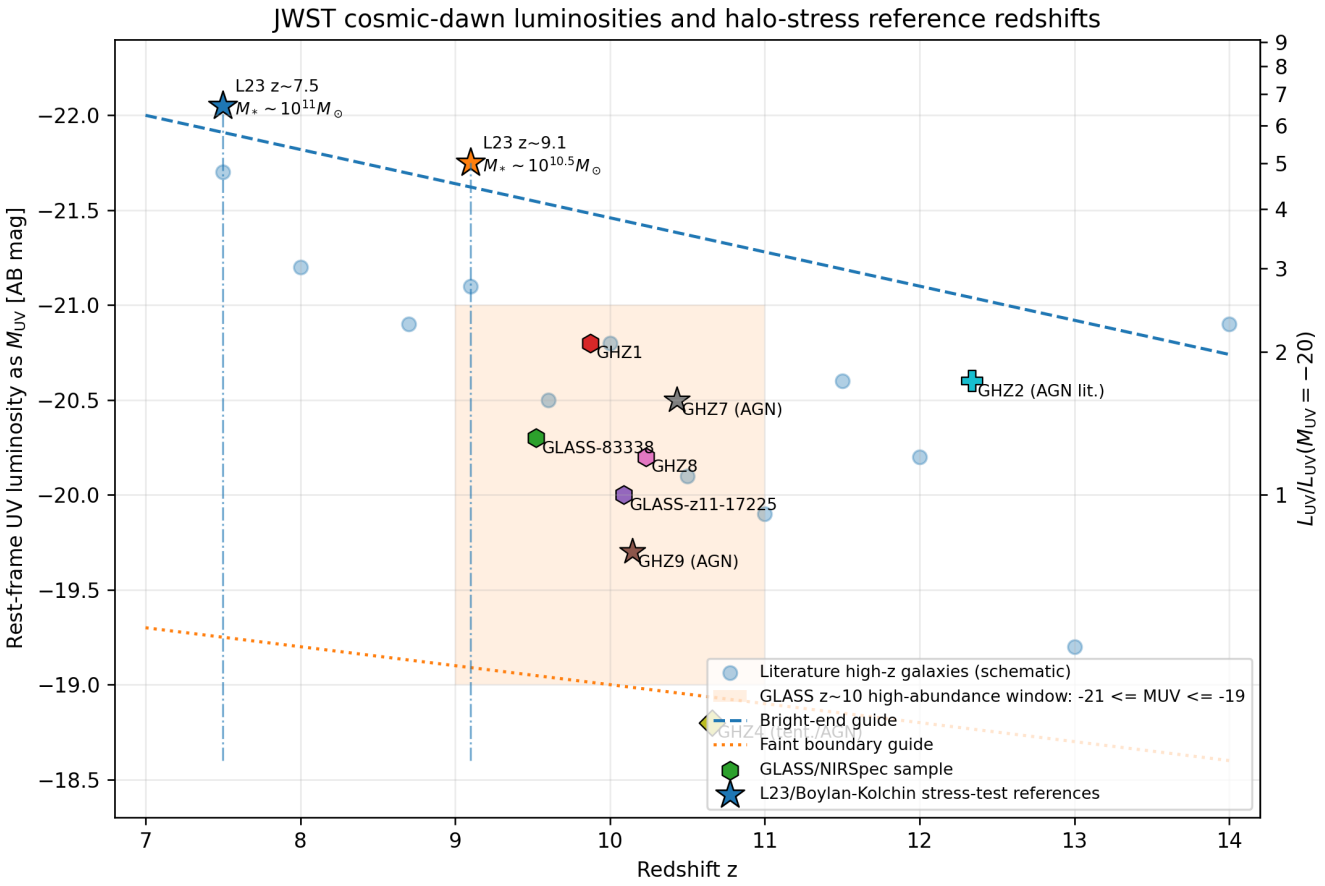


FIG. 9.— Synthesis of cosmic-dawn rest-frame UV luminosities in the redshift–$M_{\rm UV}$ plane. Representative high-redshift JWST galaxies and candidate AGN illustrate the luminosity and redshift regime relevant to the halo-to-light calculation. Brighter sources correspond to more negative $M_{\rm UV}$ (Labb
'e *et al.* 2023; Boylan-Kolchin 2023; Harikane *et al.* 2023; Atek *et al.* 2023a,b; Maiolino *et al.* 2024).

The deterministic luminosity function can consequently be written in the compact form

$$\Phi_X(M_{\rm UV}, z) = \left.\frac{\ln 10}{2.5} M_h \frac{dn_X}{dM_h}(M_h, z)\right|_{M_h = M_h(M_{\rm UV}, z)}. \quad (97)$$

Since the same halo-to-light mapping is used for ST and KST and the adopted KST correction is mass independent at fixed redshift,

$$\Phi_{\rm KST}(M_{\rm UV}, z) = F_{\rm K}(z)\Phi_{\rm ST}(M_{\rm UV}, z). \quad (98)$$

This relation separates two physically different model dependencies. Changing $\epsilon_\star$ changes the halo mass associated with a given $M_{\rm UV}$ and therefore shifts the mapping through luminosity space. The KST factor instead changes the number of halos available at that mass. A change in star-formation efficiency and a change in HMF calibration are therefore not equivalent effects.

5.6. *Comparison with Observed UV Luminosity Functions*

Figure 11 compares the predicted rest-frame UV luminosity functions at $z = 6$, 8, and 10 with representative high-redshift measurements. The model sequences use $\epsilon_\star = 0.03$, 0.10, and 0.20 for both HMF branches.

At the lower-redshift end, the COSMOS-Web determination of Franco *et al.* (2025), with median redshift $z_{\rm med} \simeq 6.41$, provides a nearby empirical benchmark for the $z = 6$ theoretical calculation. The difference in redshift is relevant because the abundance of massive halos evolves rapidly during this epoch. At $z \simeq 8$, the comparison uses the measurements of Donnan *et al.* (2023), while the $z \simeq 10$ panel uses the JWST determination of Donnan *et al.* (2024).

The separation between the ST and KST predictions grows toward high redshift according to the correction defined in Section 2.6. Because the halo-to-light relation is common to both branches, this separation directly measures the effect of the different halo abundance assigned to the same baryonic mapping. The result demonstrates that HMF calibration can become an important component of the predicted bright-galaxy abundance at cosmic dawn.

The dependence on $\epsilon_\star$ has a different origin. Increasing $\epsilon_\star$ makes a halo of fixed mass brighter and therefore allows a specified observed $M_{\rm UV}$ to be associated with a lower halo mass. Since lower-mass halos are more numerous, this can substantially increase the predicted luminosity-function amplitude at a fixed magnitude. The high-redshift UV luminosity function therefore tests the combination of baryonic conversion and cosmological halo

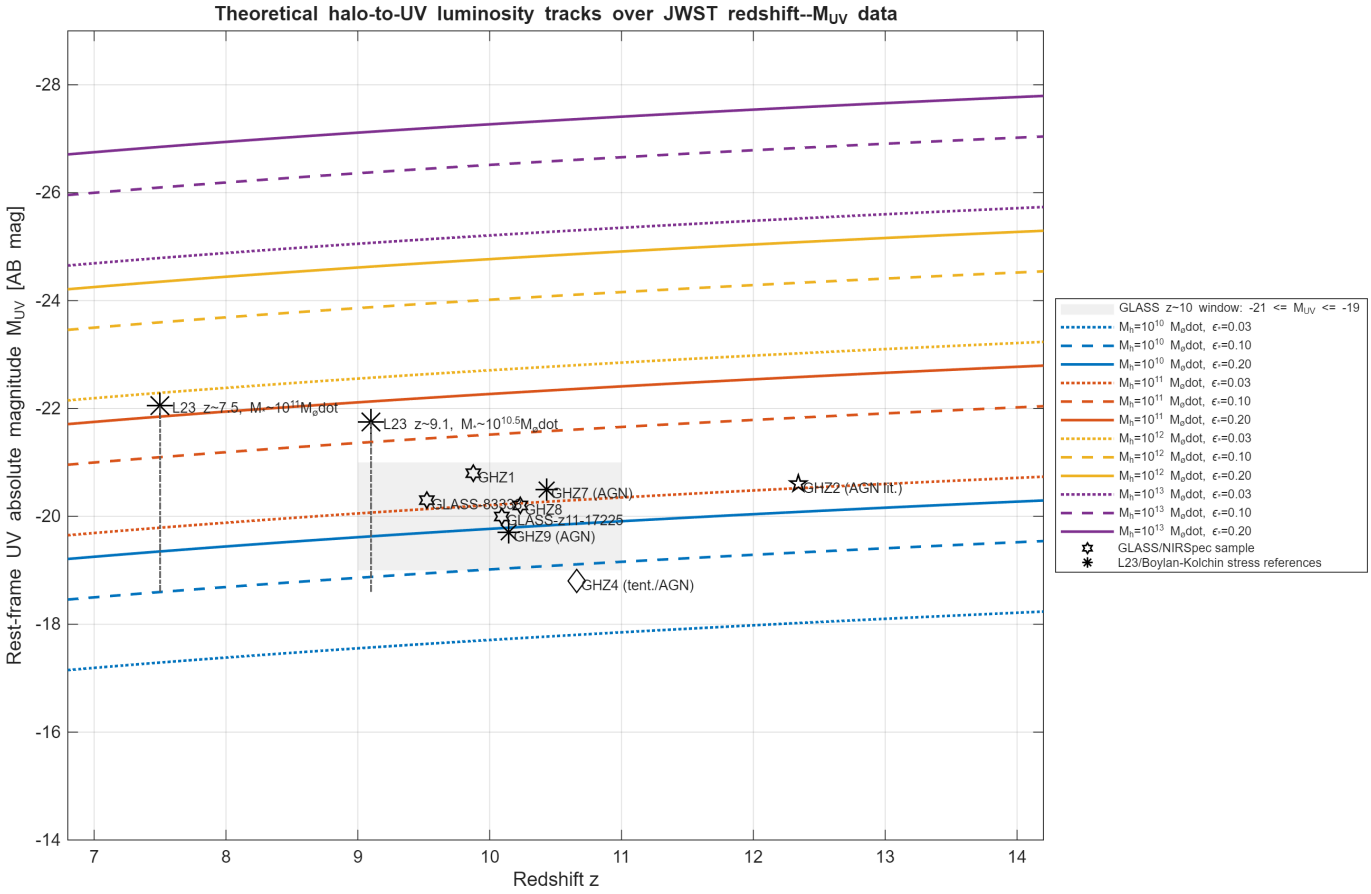


FIG. 10.— Halo-to-UV luminosity tracks in the redshift–$M_{\rm UV}$ plane for $M_h = 10^{10}$, 10^{11}, 10^{12}, and $10^{13}\,M_\odot$ and $\epsilon_\star = 0.03$, 0.10, and 0.20. For each halo mass, a common colour is used, while dotted, dashed, and solid curves denote $\epsilon_\star = 0.03$, 0.10, and 0.20, respectively. The calculation uses $M_b = f_b M_h$, SFR $= \epsilon_\star f_b M_h / t_\star$, $t_\star = 0.1 H^{-1}(z)$, and $L_{\nu,\rm UV} = \kappa_{\rm UV}$SFR. The theoretical tracks are compared with the high-redshift GLASS/NIRSpec sources of Napolitano *et al.* (2025) and with the massive galaxy candidates reported by Labb 'e *et al.* (2023) (L23), whose halo-abundance and baryonic-reservoir implications were examined by Boylan-Kolchin (2023). Increasing halo mass or stellar-conversion efficiency produces a brighter rest-frame UV magnitude, allowing the observed JWST sources to be placed directly in the context of the halo-to-light mapping.

supply rather than either ingredient in isolation.

5.7. *Scatter in the Halo-to-Light Relation*

The deterministic calculation assigns one UV magnitude to each halo mass at a fixed redshift. Real galaxies exhibit a distribution of luminosities at fixed M_h because of variations in star-formation history, gas accretion, metallicity, dust attenuation, feedback, merger history, halo assembly, and possible AGN contamination. A more general formulation introduces a conditional probability distribution

$$P(M_{\rm UV} \mid M_h, z), \tag{99}$$

normalized according to

$$\int_{-\infty}^{+\infty} P(M_{\rm UV} \mid M_h, z)\, dM_{\rm UV} = 1. \tag{100}$$

The luminosity function then becomes

$$\Phi_X(M_{\rm UV}, z) = \int_0^\infty \frac{dn_X}{dM_h}(M_h, z) \times P(M_{\rm UV} \mid M_h, z)\, dM_h. \tag{101}$$

The deterministic model corresponds to the limiting case

$$P(M_{\rm UV} \mid M_h, z) \to \delta_{\rm D}\left[M_{\rm UV} - M_{\rm UV}(M_h, z)\right]. \tag{102}$$

Scatter can be particularly important at the bright end because the HMF declines steeply with increasing mass. Upward luminosity fluctuations from the more numerous lower-mass halo population can therefore increase the number of bright sources relative to a one-to-one mapping. A full statistical comparison should consequently include scatter together with redshift uncertainties, completeness, cosmic variance, dust attenuation, bursty star formation, and survey selection.

5.8. *Interpretation of the UV Luminosity-Function Test*

The complete observational mapping may be summarized as

$$\begin{aligned} \text{JWST}\ (z, M_{\rm UV}) &\longrightarrow M_h(M_{\rm UV}, z; \epsilon_\star) \\ &\longrightarrow \frac{dn_X}{dM_h} \longrightarrow \Phi_X(M_{\rm UV}, z). \end{aligned} \tag{103}$$

The first step depends on baryonic and stellar-population physics; the second depends on the cosmological halo population. This separation explains why matching the luminosity of an individual source is necessary but not sufficient for population consistency.

The UV luminosity-function comparison extends the halo-supply analysis from individual massive or luminous objects to the population level. The measurements near

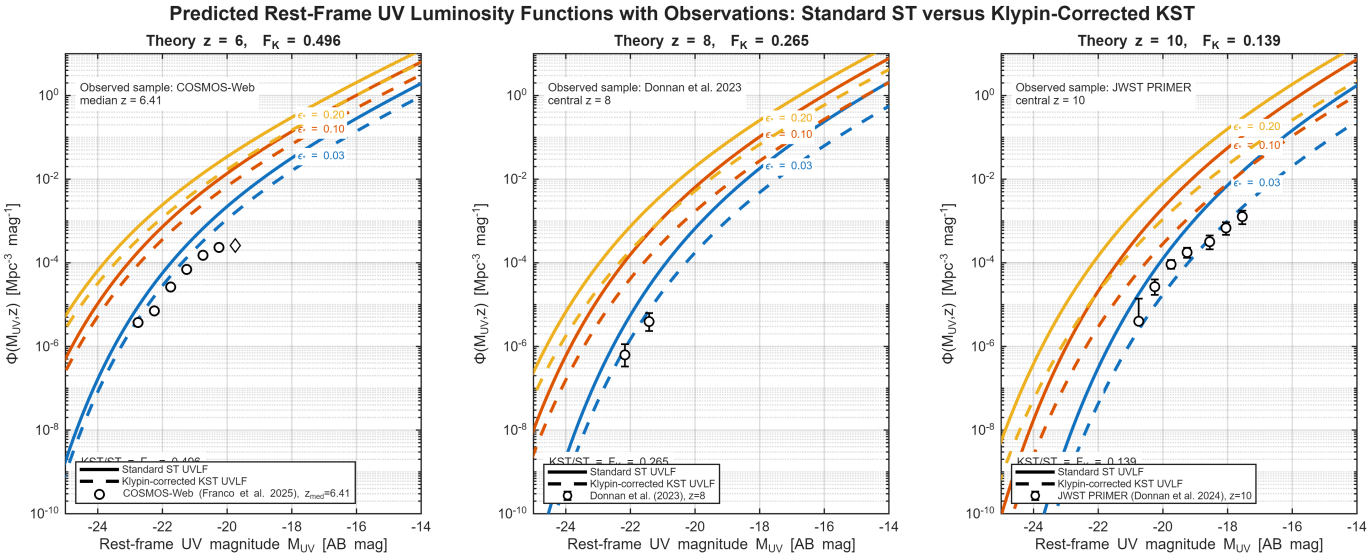


FIG. 11.— Predicted rest-frame UV luminosity functions compared with representative measurements at $z \simeq 6$–10. Solid curves show the standard Sheth–Tormen predictions and dashed curves show the corresponding KST predictions for $\epsilon_\star = 0.03$, 0.10, and 0.20. The $z = 6$ calculation is compared with COSMOS-Web measurements at $z_{\rm med} \simeq 6.41$ (Franco *et al.* 2025); the $z = 8$ calculation is compared with Donnan *et al.* (2023); and the $z = 10$ calculation is compared with Donnan *et al.* (2024). The increasing ST–KST separation toward high redshift reflects the growing sensitivity of the predicted UV-source abundance to the adopted HMF calibration.

$z \simeq 6.4$, 8, and 10 (Franco *et al.* 2025; Donnan *et al.* 2023, 2024) probe a regime in which both the halo-to-light conversion and the abundance of rare halos can materially affect the prediction. Within the deterministic model, the ST–KST difference is entirely an abundance effect, while variation of $\epsilon_\star$ changes the mapping between halo mass and observed magnitude.

The comparison is not a formal goodness-of-fit analysis. The theoretical curves use a deliberately simple halo-to-light relation, whereas the observational measurements are affected by selection functions, photometric and spectroscopic redshift uncertainties, completeness, survey volume, cosmic variance, and possible AGN contributions to the UV continuum. On the theoretical side, stellar-population modeling, metallicity, dust attenuation, feedback, bursty star formation, and scatter in the halo–luminosity relation can all modify the predicted luminosity function.

The appropriate interpretation is therefore a quantitative test of the combined cosmological and astrophysical framework. A discrepancy between a single deterministic curve and the measured luminosity function does not by itself identify its origin as cosmological. Conversely, adjusting the halo-to-light mapping cannot create additional dark-matter halos; the cosmological supply remains constrained by the HMF. The most informative comparison is consequently one in which uncertainties in both the baryonic mapping and the halo abundance are propagated together.

The quantitative KST luminosity-function comparison is restricted to the calibration interval $z \leq 10$ specified in Section 2.6.1. Halo-to-light relations and observational redshift–luminosity diagrams may be considered at higher redshift, but a KST abundance prediction beyond this boundary is an extrapolation rather than a simulation-calibrated result.

Together with the massive-galaxy and AGN abundance tests, the UV luminosity function completes the three observational applications of the common halo framework. The resulting comparison separates the cosmological abundance of potential hosts from the baryonic and black-hole processes that determine which of those hosts become observable at cosmic dawn.

6. DISCUSSION AND COSMOLOGICAL IMPLICATIONS

The high-redshift galaxy and AGN populations observed by JWST provide a sensitive test of the connection between cosmological structure formation and the baryonic processes that make dark-matter halos observable. The three applications considered in this work—massive galaxies, AGN host abundance, and the rest-frame UV luminosity function—probe different observables, but they share the same underlying question: does the cosmological halo population provide a sufficiently large reservoir of hosts once the mapping from halo mass to the observed population is specified?

This distinction separates the problem into two coupled components. The cosmological component determines the abundance and mass distribution of halos. The astrophysical component determines how stellar mass, black-hole activity, and UV luminosity are assigned to those halos. At low redshift, moderate changes in either component may have relatively limited effects on predicted number densities. At cosmic dawn, however, massive systems occupy the rare, high-ν tail of the halo distribution, where the abundance changes rapidly with both halo mass and redshift. Uncertainties in the observable-to-halo mapping and in the HMF calibration can therefore be strongly amplified.

The standard Sheth–Tormen (ST) HMF provides the principal analytic baseline throughout the analysis. The Bolshoi/Klypin-corrected ST (KST) prescription provides an illustrative simulation-motivated test of the sensitivity to high-redshift HMF calibration. Since the KST factor in the adopted implementation is independent of halo mass at fixed redshift, it changes the available halo abundance without changing the common power spectrum, mass

variance, peak-height calculation, or the baryonic and luminosity mappings. This separation makes it possible to identify which conclusions arise from the cosmological halo supply and which arise from the astrophysical mapping.

6.1. *Rare Halos and the High-Redshift Host Supply*

The mass variance and peak-height calculations show that increasingly massive halos at high redshift correspond to increasingly rare fluctuations in the primordial density field. This is the fundamental reason that the earliest massive galaxies and luminous AGN can provide stringent tests of structure formation. Once a source is associated with a minimum host mass $M_{\rm min}$, the relevant cosmological quantity is the cumulative abundance

$$n_X(> M_{\rm min}, z), \qquad X \in \{\mathrm{ST}, \mathrm{KST}\}. \tag{104}$$

The steepness of the rare-halo tail has an important consequence: a modest change in the inferred host mass can produce a much larger change in the predicted abundance. The observational significance of an apparently extreme source therefore cannot be assessed from its luminosity or stellar mass alone. It depends on how those quantities map into halo mass and on the HMF used to calculate the abundance of such halos.

Within the calibrated redshift interval, the KST prescription lowers the high-redshift halo supply relative to the ST baseline. The effect becomes progressively more important toward cosmic dawn. Because the correction has already been defined quantitatively in Section 2.6, it is useful here to emphasize its interpretation rather than repeat its numerical definition: the KST branch represents a controlled change in halo abundance, not a modification of the underlying linear density field or of the halo-to-observable physics.

This distinction is especially relevant when considering the most extreme objects. A large stellar mass, black-hole mass, or UV luminosity may imply a rare host under one astrophysical mapping but a substantially more common host under another. Conversely, for a fixed host requirement, different HMF calibrations can predict materially different numbers of eligible systems. High-redshift abundance tests therefore constrain the combination of these ingredients rather than either one in isolation.

6.2. *Massive Galaxies as Baryonic-Reservoir Tests*

The massive-galaxy application is governed first by the finite baryonic reservoir associated with a halo. The relation

$$M_\star \leq \epsilon_\star f_b M_h \tag{105}$$

provides a direct consistency condition between an inferred stellar mass and its host. The limiting value $\epsilon_\star = 1$ represents an absolute baryonic ceiling; realistic stellar-conversion efficiencies are expected to be smaller.

The importance of this constraint increases at high redshift because the halo mass required to support a large stellar mass may lie on the rapidly declining high-mass tail. Lowering $\epsilon_\star$ raises the required host mass, thereby reducing the number of eligible halos. The abundance constraint is therefore not determined by the baryon fraction alone: it depends jointly on the stellar-mass estimate, the adopted conversion efficiency, and the cosmological abundance of the resulting host population (Labb 'e *et al.* 2023; Boylan-Kolchin 2023).

The cumulative mass-density test provides a complementary integral constraint. Even if an individual halo can in principle contain the required stellar mass, the total collapsed matter contained in all eligible halos must be sufficient to support the observed stellar-mass density. The individual host test and the integrated mass-reservoir test thus probe different aspects of the same physical requirement.

These considerations also illustrate why the most massive JWST systems should be treated as quantitative stress tests rather than as binary cosmological falsification criteria. Stellar masses at these redshifts depend on stellar-population synthesis, star-formation history, dust, nebular emission, redshift, and possible AGN contamination. Lensing magnification, survey volume, completeness, and cosmic variance can additionally affect the inferred population abundance. Because the halo abundance is so steep, relatively modest changes in these quantities can produce appreciable shifts in the inferred cosmological constraint.

6.3. *AGN Abundance and Early Black-Hole Growth*

The AGN application introduces additional astrophysical degrees of freedom. For a threshold host model, the observable abundance can be expressed as

$$n_{\mathrm{AGN},X}(z) = f_{\rm occ} f_{\rm duty} n_X(> M_{\rm min}, z), \tag{106}$$

where $f_{\rm occ}$ is the black-hole occupation fraction and $f_{\rm duty}$ is the active fraction. The host threshold itself depends on the mapping between AGN luminosity, black-hole mass, Eddington ratio, and halo mass.

A pure abundance measurement therefore cannot uniquely determine all of these quantities. A low AGN number density may indicate rare massive hosts, a low occupation fraction, a short duty cycle, or some combination of the three. Similarly, assigning a luminous AGN to a very massive host can make the available halo population extremely small, whereas a lower characteristic host mass can substantially relax the halo-supply requirement.

The host-abundance calculation also has implications for early black-hole growth. Light stellar-remnant seeds require substantially more subsequent growth than heavy-seed scenarios, while the limited time available at high redshift places additional demands on the accretion history. The halo calculation does not distinguish among seed-formation mechanisms, but it constrains the number of environments in which a successful growth history can occur. Depending on the inferred black-hole and host masses, viable scenarios may require sustained near-Eddington or super-Eddington accretion, heavier initial seeds, elevated black-hole-to-halo mass ratios, or lower characteristic host masses (Volonteri 2010; Inayoshi *et al.* 2020).

Clustering provides an important complementary observable because it probes the characteristic host mass through halo bias. More massive and rarer hosts generally imply stronger large-scale clustering. Abundance and clustering therefore constrain different aspects of the AGN–halo connection: abundance measures the available number of hosts, whereas clustering constrains their typical rarity. Under the mass-independent KST rescaling used here, the common abundance factor cancels from a

normalized effective-bias calculation when the same bias relation and occupation model are used. The KST prescription therefore changes the predicted host abundance without, by itself, changing the normalized AGN bias.

6.4. *UV Luminosity Functions as Population-Level Tests*

The UV luminosity-function application moves the comparison from individual extreme systems to the population level. A deterministic halo-to-light model assigns a UV magnitude to each halo mass through the baryonic conversion efficiency, star-formation timescale, and UV luminosity calibration. The HMF then determines how many halos populate each luminosity interval.

This separation can be represented schematically as

$$\begin{aligned} M_h &\longrightarrow M_{\rm UV}(M_h, z; \epsilon_\star), \\ \frac{dn_X}{dM_h} &\longrightarrow \Phi_X(M_{\rm UV}, z). \end{aligned} \tag{107}$$

Changing $\epsilon_\star$ modifies the luminosity assigned to a halo and hence the halo mass associated with a fixed observed magnitude. Changing the HMF calibration modifies the number of halos available at that mass. These are physically distinct effects and should not be absorbed into a single efficiency parameter.

The comparison with high-redshift luminosity-function measurements near $z \simeq 6.4$, 8, and 10 (Franco *et al.* 2025; Donnan *et al.* 2023, 2024) illustrates why both effects become important toward cosmic dawn. Increasing the stellar-conversion efficiency allows a given UV luminosity to be produced by a lower-mass and more abundant halo. The KST abundance correction acts in the opposite direction by reducing the number of halos available to populate the luminosity function. The observed bright-end abundance therefore constrains the combination of halo-to-light physics and cosmological halo supply.

A deterministic relation is useful for exposing these dependencies, but real galaxies exhibit intrinsic scatter in luminosity at fixed halo mass. The more general prediction is

$$\begin{aligned} \Phi_X(M_{\rm UV}, z) = \int_0^\infty & \frac{dn_X}{dM_h}(M_h, z) \\ & \times P(M_{\rm UV} \mid M_h, z)\, dM_h. \end{aligned} \tag{108}$$

Scatter is especially important at the bright end because numerous lower-mass halos can scatter toward higher luminosities. A realistic forward model should therefore distinguish intrinsic halo-to-light scatter from observational uncertainties in flux, redshift, completeness, and inferred number density.

6.5. *The Role of Halo-Mass-Function Calibration*

The comparison between ST and KST highlights a broader issue: the HMF itself is a theoretical and numerical ingredient in high-redshift abundance tests. Analytic collapse prescriptions are not exact descriptions of the halo population, and simulation-calibrated mass functions depend on halo finder, mass definition, cosmological parameters, numerical resolution, simulation volume, and calibration redshift (Tinker *et al.* 2008; Klypin *et al.* 2011).

This issue becomes particularly important for rare objects. A calibration difference that appears moderate in the bulk of the halo population can produce a substantial change in the inferred abundance of the most massive systems. Theoretical uncertainty in the HMF must therefore be considered alongside observational and baryonic uncertainties when assessing early galaxy and AGN populations.

The ST–KST comparison should not be interpreted as exhausting the range of possible HMF calibrations. Rather, it demonstrates quantitatively that the choice of halo-abundance prescription can materially affect the inferred high-redshift host reservoir. A precision analysis would compare multiple modern simulation-calibrated HMFs using consistent halo-mass definitions and cosmological parameters and would propagate their calibration uncertainties through the galaxy and AGN mappings.

The halo-mass definition is part of this consistency requirement. A mass inferred observationally or adopted in a halo-occupation model must be matched to the mass convention used in the numerical HMF calibration. Differences among virial, friends-of-friends, and spherical-overdensity masses can become important in the rare-halo regime, where even modest changes in mass can lead to large abundance differences.

6.6. *Calibration Boundary at $z = 10$*

The quantitative KST calculations are restricted to the calibration interval specified in Section 2.6.1,

$$0 \leq z \leq 10. \tag{109}$$

The analytic correction can be evaluated mathematically at larger redshift, but such values constitute extrapolations rather than simulation-calibrated predictions.

This distinction is important because the high-redshift correction becomes increasingly restrictive as z increases. Extending it beyond its calibrated domain without additional numerical validation could therefore create an artificially strong abundance constraint. Observed systems at $z > 10$ remain important probes of early structure formation and of the halo-to-light mapping, but they should not be used as the basis for a calibrated KST exclusion.

Direct calibration at these redshifts will require simulations with sufficient volume to sample rare massive halos while maintaining the mass resolution needed to follow their progenitors and environments. Consistent halo definitions and controlled comparisons among numerical codes will be equally important.

6.7. *Dominant Sources of Uncertainty*

The interpretation of high-redshift abundance tests depends on uncertainties at several levels. On the cosmological side, relevant ingredients include the normalization and shape of the matter power spectrum, linear growth, transfer-function modeling, halo definition, and numerical calibration of the HMF. For the framework considered here, HMF calibration is particularly important because the observations probe the rapidly varying rare-halo tail.

The galaxy mapping introduces uncertainties in stellar-population synthesis, the stellar initial mass function, star-formation history, stellar conversion efficiency, metallicity, nebular emission, dust attenuation, feedback, and scatter between halo mass and luminosity. For AGN, additional uncertainties arise from black-hole mass estimation, bolometric corrections, Eddington ratios, obscu-

ration, black-hole occupation, duty cycle, and the relation between black-hole and halo mass.

Observational uncertainties include photometric and spectroscopic redshifts, flux measurements, completeness corrections, source classification, gravitational magnification, survey volume. These uncertainties are not independent. For example, an AGN contribution can alter an inferred stellar mass as well as a UV luminosity, while a redshift revision changes both the inferred source properties and the predicted halo abundance.

The rare-halo tail amplifies the combined effect. A relatively small shift in an inferred stellar mass, Eddington ratio, or characteristic host mass may correspond to a much larger change in the predicted number of halos. Strong cosmological conclusions therefore require a joint treatment of observational errors, astrophysical scatter, and HMF calibration rather than variation of only one ingredient at a time.

6.8. *Do the Current Data Require Physics Beyond ΛCDM?*

The present calculations do not require a departure from standard ΛCDM. Instead, the JWST populations probe regions of parameter space in which the predicted halo supply can become small and strongly sensitive to the adopted host mapping and HMF calibration. The resulting observations are therefore increasingly stringent stress tests of the combined cosmological and astrophysical framework.

This interpretation is important because an abundance discrepancy does not uniquely identify its physical origin. A mismatch may arise from an overestimated stellar or black-hole mass, an incorrect characteristic host mass, an incomplete treatment of scatter, an inappropriate duty cycle or occupation fraction, an HMF calibration error, or a genuine shortcoming of the cosmological model. These possibilities must be distinguished before a departure from ΛCDM can be inferred.

If future observations, improved halo calibration, and more realistic astrophysical modeling establish a statistically persistent discrepancy, cosmological extensions could then be investigated. Possibilities include changes to the primordial power spectrum, non-Gaussian initial conditions, early-dark-energy scenarios, or modified gravity. Such extensions are not required or fitted in the present analysis. Any viable alternative would also have to remain consistent with the cosmic microwave background, large-scale structure, gravitational lensing, nucleosynthesis, and the other successful tests of the standard cosmological model.

6.9. *Observational and Theoretical Tests Ahead*

Progress on the observational side will come from larger survey volumes, deeper spectroscopy, improved stellar-mass measurements, more secure AGN classification, and better characterization of selection functions and redshift distributions. Clustering and gravitational lensing are especially valuable because they can constrain characteristic host-halo masses more directly than abundance measurements alone.

JWST will continue to provide deep measurements of the earliest galaxy and AGN populations, while wide-field and multiwavelength observations from facilities such as the Nancy Grace Roman Space Telescope, Euclid, Athena, the Square Kilometre Array, and next-generation extremely large telescopes can extend the available volumes and provide complementary constraints on stellar populations, black-hole activity, environments, and clustering.

On the theoretical side, larger-volume and higher-resolution simulations at $z \gtrsim 10$ are needed to calibrate the rare-halo population directly. Forward models should replace single-valued halo-to-light relations with conditional distributions that include luminosity scatter, evolving star-formation efficiency, bursty star formation, dust, feedback, and AGN contamination. AGN calculations should similarly incorporate distributions of black-hole mass, Eddington ratio, obscuration, occupation, and duty cycle.

A particularly powerful approach will be to combine multiple observables. Number densities constrain the available host population; luminosity functions constrain the distribution of observable output; clustering constrains characteristic host mass; lensing can test halo mass more directly; and spectroscopy constrains redshift, stellar populations, ionization state, and AGN activity. Joint analysis of these observables can reduce degeneracies that cannot be resolved by any single measurement.

6.10. *Cosmological Interpretation*

The physical sequence connecting primordial fluctuations to the observed high-redshift populations may be summarized as

$$\begin{aligned} P(k) &\longrightarrow \sigma(M,z) \longrightarrow \nu(M,z) \longrightarrow \frac{dn_X}{dM} \\ &\longrightarrow \{n_X(>M,z),\, \rho_{h,X}(>M,z)\} \\ &\longrightarrow \{M_\star,\, n_{\rm AGN},\, M_{\rm UV}\} \longrightarrow \Phi(M_{\rm UV},z). \end{aligned} \tag{110}$$

Three conclusions follow from this framework. First, the most massive high-redshift galaxies and luminous AGN probe the rare-halo regime in which small changes in host mass or redshift can produce large abundance changes. Second, the calibration of the HMF is itself an important component of the prediction; the ST–KST comparison demonstrates that uncertainty in the high-redshift halo supply can materially affect massive-galaxy, AGN, and UV luminosity-function tests. Third, the cosmological halo supply and the astrophysical observable-to-halo mapping must be treated as distinct but coupled components of the inference.

The emerging JWST populations therefore provide quantitative stress tests of ΛCDM structure formation and of the baryonic and black-hole physics that connect halos to observable sources. The most robust cosmological conclusions will come from discrepancies that persist after observational uncertainties, stochastic halo-to-light mappings, host-halo inference, and high-redshift HMF calibration uncertainties are treated jointly. In this sense, the earliest galaxies and AGN provide a direct observational bridge between primordial density fluctuations, nonlinear gravitational collapse, baryonic conversion, and black-hole growth.

7. SUMMARY AND CONCLUSIONS

JWST observations of massive galaxies and luminous active galactic nuclei during the first billion years have

made the high-redshift halo population an increasingly direct probe of cosmological structure formation. The analysis presented here connects the linear matter fluctuation spectrum to halo formation and then to three complementary observational tests: the baryonic reservoir available to massive galaxies, the abundance of halos capable of hosting luminous AGN, and the rest-frame ultraviolet luminosity function of high-redshift galaxies.

The calculation begins with a common Planck-like ΛCDM cosmology and constructs the linear matter power spectrum, mass variance, peak height, and halo abundance. The Sheth–Tormen (ST) mass function is used as the principal analytic baseline. A Bolshoi/Klypin-corrected ST prescription (KST) is carried as an illustrative simulation-motivated alternative in order to quantify the sensitivity of the high-redshift conclusions to HMF calibration. The two branches share the same underlying power spectrum, growth history, mass variance, peak-height definition, and astrophysical mappings; they differ only in the adopted halo abundance. This separation allows HMF uncertainty to be distinguished from uncertainties in the conversion of halos into observable galaxies and AGN.

The massive-galaxy test shows that an inferred stellar mass must satisfy both an individual baryonic-reservoir condition and a population-level abundance condition. For a halo of mass M_h,

$$M_\star \le \epsilon_\star f_b M_h, \qquad 0 < \epsilon_\star \le 1, \tag{111}$$

where $\epsilon_\star = 1$ represents an absolute baryonic ceiling rather than a realistic star-formation efficiency. As the required host mass increases, the rapidly declining rare-halo tail makes the corresponding abundance constraint progressively stronger. The cumulative halo-mass-density calculation provides an additional integral test by asking whether the total matter and baryonic reservoir contained in the eligible halo population can support the inferred stellar-mass density.

For AGN, halo abundance provides an upper envelope rather than a direct prediction of the observable population. The expected number density also depends on black-hole occupation, duty cycle, and the relation between AGN luminosity, black-hole mass, Eddington ratio, and host-halo mass. In the simplified threshold description,

$$n_{\mathrm{AGN},X}(z) = f_{\mathrm{occ}} f_{\mathrm{duty}}\, n_X(>M_{\mathrm{min}}, z), \qquad X \in \{\mathrm{ST}, \mathrm{KST}\}. \tag{112}$$

Consequently, a shortage of sufficiently massive halos cannot be alleviated by reducing the occupation fraction or duty cycle; those factors can only lower the predicted active population. Conversely, uncertainty in the characteristic host mass can substantially alter the abundance constraint because the calculation samples the steep high-mass tail. Clustering and lensing measurements are therefore valuable complementary probes of the host-halo masses associated with high-redshift AGN.

The UV luminosity-function calculation extends the analysis from individual extreme objects to the galaxy population as a whole. A deterministic halo-to-light relation specifies the UV luminosity associated with a halo of given mass, redshift, and star-formation efficiency, while the HMF determines how many such halos exist. These two ingredients answer different physical questions. Increasing the stellar-conversion efficiency can lower the halo mass required to produce a specified luminosity; changing the HMF calibration changes the abundance of halos available at that mass. The comparison with representative measurements near $z \simeq 6.4$, 8, and 10 therefore demonstrates that high-redshift luminosity functions constrain both baryonic physics and the cosmological halo supply.

Across all three tests, the same general result emerges: the interpretation of the earliest massive and luminous systems depends sensitively on the mapping between an observable and its host halo because these systems occupy the rare, high-ν regime. Relatively modest changes in inferred stellar mass, star-formation efficiency, Eddington ratio, or characteristic host mass can produce much larger changes in the predicted halo abundance. HMF calibration adds a separate source of uncertainty. The ST–KST comparison demonstrates that this uncertainty can materially affect the inferred high-redshift host reservoir and should not be absorbed into an astrophysical efficiency parameter.

The KST prescription is used quantitatively only within its adopted simulation-calibrated interval, $0 \le z \le 10$. Although its analytic form can be evaluated at larger redshift, such use is extrapolative. Objects at $z > 10$ remain important probes of early structure formation, but robust HMF constraints in that regime require simulations that directly calibrate the rare-halo population at those epochs.

The present results do not establish that current JWST observations require a departure from standard ΛCDM. Instead, they identify the combinations of halo abundance, host mass, baryonic conversion, black-hole occupation, duty cycle, and halo-to-light mapping that are most demanding within the standard framework. The appropriate interpretation of the most extreme systems is therefore as quantitative stress tests of cosmological structure formation and of the astrophysical assumptions used to connect halos with observable sources.

Future progress will require these components to be constrained jointly. Larger survey volumes and improved spectroscopy will refine galaxy and AGN number densities, stellar masses, redshifts, and source classifications. Clustering and lensing can constrain characteristic host masses. On the theoretical side, higher-redshift HMF calibrations and stochastic halo-to-observable models are needed, including scatter, evolving star-formation efficiency, bursty star formation, dust and feedback for galaxies, and distributions of black-hole mass, Eddington ratio, occupation, obscuration, and duty cycle for AGN.

The principal value of the framework is that it keeps these ingredients physically distinct while placing them in a common abundance calculation. The chain

$$\begin{aligned} P(k) &\longrightarrow \sigma(M,z) \longrightarrow \nu(M,z) \longrightarrow \frac{dn_X}{dM} \\ &\longrightarrow \{n_X(>M,z),\, \rho_{h,X}(>M,z)\} \\ &\longrightarrow \{M_\star,\, n_{\mathrm{AGN}},\, M_{\mathrm{UV}},\, \Phi(M_{\mathrm{UV}},z)\} \end{aligned} \tag{113}$$

provides a transparent connection from primordial density fluctuations to nonlinear collapse and ultimately to the galaxies and AGN observed at cosmic dawn. As the observational samples and theoretical calibrations improve,

this combined approach can provide increasingly stringent tests of the standard structure-formation picture while making clear whether any emerging discrepancy originates primarily in the cosmological halo supply, the astrophysical mapping, or the interaction between the two.

ACKNOWLEDGEMENTS

The authors gratefully acknowledge the support of the Johns Hopkins University Whiting School EP Applied Physics Program. R.S. also acknowledges the support of the Johns Hopkins University Applied Physics Laboratory.

DATA AVAILABILITY

The numerical results presented in this work are derived from the analytic models and observational datasets cited in the text. The numerical code used to generate the theoretical calculations and figures is available from the corresponding author upon reasonable request.

REFERENCES

P. J. E. Peebles, *The Large-Scale Structure of the Universe* (Princeton University Press, 1980).
J. A. Peacock, *Cosmological Physics* (Cambridge University Press, 1999).
S. Dodelson and F. Schmidt, *Modern Cosmology*, 2nd ed. (Academic Press, 2020).
Planck Collaboration VI, A&A **641**, A6 (2020).
J. M. Bardeen, J. R. Bond, N. Kaiser, and A. S. Szalay, ApJ **304**, 15 (1986).
D. J. Eisenstein and W. Hu, ApJ **496**, 605 (1998).
J. E. Gunn and J. R. Gott, ApJ **176**, 1 (1972).
W. H. Press and P. Schechter, ApJ **187**, 425 (1974).
J. R. Bond, S. Cole, G. Efstathiou, and N. Kaiser, ApJ **379**, 440 (1991).
C. Lacey and S. Cole, MNRAS **262**, 627 (1993).
R. K. Sheth and G. Tormen, MNRAS **308**, 119 (1999).
J. L. Tinker, A. V. Kravtsov, A. Klypin, *et al.*, ApJ **688**, 709 (2008).
J. Kormendy and L. C. Ho, ARA&A **51**, 511 (2013).
M. Volonteri, A&ARv **18**, 279 (2010).
K. Inayoshi, E. Visbal, and Z. Haiman, ARA&A **58**, 27 (2020).
I. Labb
'e *et al.*, Nature **616**, 266 (2023).
M. Boylan-Kolchin, Nature Astronomy **7**, 731 (2023).
H. Atek *et al.*, MNRAS **519**, 1201 (2023a).
H. Atek *et al.*, MNRAS **524**, 5486 (2023b).
Y. Harikane *et al.*, ApJ **959**, 39 (2023).
D. D. Kocevski *et al.*, ApJL **954**, L4 (2023).
R. Maiolino *et al.*, Nature **626**, 271 (2024).
L. Napolitano *et al.*, A&A **693**, A50 (2025).
C. T. Donnan *et al.*, MNRAS **518**, 6011 (2023).
C. T. Donnan *et al.*, MNRAS **533**, 3222 (2024).
M. Franco *et al.*, arXiv e-prints (2025), arXiv:2508.04791.
A. A. Klypin, S. Trujillo-Gomez, and J. R. Primack, ApJ **740**, 102 (2011).
A. J. Benson, E. O. Nadler, X. Du, and V. Gluscevic, arXiv e-prints (2026), arXiv:2606.12137 [astro-ph.CO].
H. J. Mo, F. C. van den Bosch, and S. D. M. White, *Galaxy Formation and Evolution* (Cambridge University Press, 2010).
R. K. Sheth, H. J. Mo, and G. Tormen, MNRAS **323**, 1 (2001).
P. S. Behroozi, R. H. Wechsler, and C. Conroy, ApJ **770**, 57 (2013).
B. P. Moster, T. Naab, and S. D. M. White, MNRAS **428**, 3121 (2013).
P. Dayal *et al.*, A&A **697**, A211 (2025).
R. J. Bouwens *et al.*, AJ **162**, 47 (2021).
S. L. Finkelstein and M. B. Bagley, ApJ **938**, 25 (2022).
R. S. Somerville and R. Dav
'e, ARA&A **53**, 51 (2015)

APPENDIX

A. DERIVING THEORETICAL UV LUMINOSITY FUNCTIONS FROM THE STANDARD AND KLYPIN-CORRECTED SHETH–TORMEN HALO MASS FUNCTIONS

This appendix completes the bridge between the theoretical halo mass function and the observable rest-frame ultraviolet (UV) luminosity function measured in high-redshift galaxy surveys. The main text introduced the halo-to-light mapping as an intermediate diagnostic. Here we formulate the luminosity function in parallel for two halo-abundance prescriptions: the standard Sheth–Tormen (ST) halo mass function and the Bolshoi-calibrated, Klypin-corrected Sheth–Tormen (KST) halo mass function.

For a general halo mass function dn_X/dM_h, where $X \in \{\mathrm{ST}, \mathrm{KST}\}$, the UV luminosity function is

$$\Phi_X(M_{\mathrm{UV}}, z) = \int \frac{dn_X}{dM_h}(M_h, z)\, P(M_{\mathrm{UV}}|M_h, z)\, dM_h, \tag{A1}$$

where $P(M_{\mathrm{UV}}|M_h, z)$ is the conditional probability that a halo of mass M_h at redshift z is observed with UV absolute magnitude M_{UV}.

The purpose of this appendix is not to construct a complete semi-analytic galaxy-formation model. Rather, it provides a transparent framework showing how both the standard ST and KST halo mass functions propagate through the same halo-to-light model. This formulation is designed to support direct side-by-side numerical comparisons of

$$\Phi_{\mathrm{ST}}(M_{\mathrm{UV}}, z) \qquad \text{and} \qquad \Phi_{\mathrm{KST}}(M_{\mathrm{UV}}, z), \tag{A2}$$

while keeping all baryonic, stellar, duty-cycle, and scatter assumptions identical.

A.1. *Standard and Klypin-corrected Sheth–Tormen halo mass functions*

The halo-abundance calculation used throughout this work begins with the standard Sheth–Tormen (ST) mass function (Sheth and Tormen 1999; Sheth *et al.* 2001),

$$\frac{dn_{\mathrm{ST}}}{dM_h}(M_h, z) = \frac{\bar{\rho}_m}{M_h}\, f_{\mathrm{ST}}(\nu) \left| \frac{d\nu}{dM_h} \right|, \tag{A3}$$

where $\bar{\rho}_m$ is the mean comoving matter density and the peak-height variable is defined by

$$\nu(M_h, z) = \frac{\delta_c}{\sigma(M_h, z)} = \frac{\delta_c}{D(z)\sigma(M_h, 0)}. \tag{A4}$$

Here $\delta_c \simeq 1.686$ is the spherical-collapse threshold and $D(z)$ is the scale-independent linear growth factor, normalized such that $D(0) = 1$.

For the spatially flat ΛCDM cosmology adopted in this work, the growth factor is evaluated from

$$D(a) = \frac{E(a)\displaystyle\int_0^a \frac{da'}{a'^3 E^3(a')}}{E(1)\displaystyle\int_0^1 \frac{da'}{a'^3 E^3(a')}}, \tag{A5}$$

where

$$E(a) = \frac{H(a)}{H_0} = \left(\Omega_{m,0}a^{-3} + \Omega_{\Lambda,0}\right)^{1/2}, \tag{A6}$$

with $a = (1+z)^{-1}$. The common multiplicative factor $5\Omega_{m,0}/2$ in the integral solution cancels when the growth function is normalized to $D(1) = D(z = 0) = 1$. Thus the calculation does not assume the Einstein–de Sitter approximation $D(z) = (1 + z)^{-1}$; the full flat-ΛCDM growth history is used.

The Sheth–Tormen multiplicity function is

$$f_{\rm ST}(\nu) = A\sqrt{\frac{2a_{\rm ST}}{\pi}}\,\nu\left[1 + \left(a_{\rm ST}\nu^2\right)^{-p}\right]\exp\left(-\frac{a_{\rm ST}\nu^2}{2}\right), \tag{A7}$$

with the standard parameters

$$A = 0.3222, \qquad a_{\rm ST} = 0.707, \qquad p = 0.3. \tag{A8}$$

The notation $a_{\rm ST}$ is used here to distinguish the Sheth–Tormen parameter from the cosmological scale factor a.

The variance entering equation (A4) is calculated from the linear matter power spectrum,

$$\sigma^2(M_h, z) = \frac{1}{2\pi^2}\int_0^\infty k^2 P(k, z)W^2(kR)\,dk, \tag{A9}$$

where $W(kR)$ is the Fourier-space spherical top-hat window function and

$$M_h = \frac{4\pi}{3}\bar{\rho}_m R^3. \tag{A10}$$

Equivalently, with scale-independent linear growth, $P(k, z) = D^2(z)P(k, 0)$ and hence $\sigma(M_h, z) = D(z)\sigma(M_h, 0)$.

The Bolshoi simulation analysis of Klypin *et al.* (2011) found that the standard ST expression increasingly overpredicts the abundance of distinct spherical-overdensity halos toward high redshift. We therefore adopt the redshift-dependent correction

$$F_{\rm K}(z) = \frac{[5.501D(z)]^4}{1 + [5.500D(z)]^4}, \tag{A11}$$

using the same normalized ΛCDM growth factor $D(z)$ defined above.

The Klypin-corrected Sheth–Tormen (KST) halo mass function used in this work is therefore

$$\boxed{\frac{dn_{\rm KST}}{dM_h}(M_h, z) = F_{\rm K}(z)\frac{dn_{\rm ST}}{dM_h}(M_h, z)} \tag{A12}$$

or, equivalently,

$$f_{\rm KST}(\nu, z) = F_{\rm K}(z)f_{\rm ST}(\nu). \tag{A13}$$

This distinction is important conceptually. Because $F_{\rm K}$ depends explicitly on redshift through $D(z)$, $f_{\rm KST}$ is not a universal multiplicity function of ν alone. Moreover, in the implementation adopted here $F_{\rm K}$ is independent of halo mass at fixed redshift. The correction therefore changes the normalization of the halo abundance but does not alter the mass dependence of the underlying ST curve at that redshift. It also does not modify the matter power spectrum, $\sigma(M, z)$, the peak-height definition, or the baryonic halo-to-light mapping.

The representative numerical values of $F_{\rm K}(z)$ are given in Equation (37) of Section 2.6.

Thus the corresponding ST-to-KST abundance ratios are approximately

$$\frac{n_{\rm ST}}{n_{\rm KST}} \simeq 1.27, \quad 2.02, \quad 3.77, \quad 7.18 \qquad \text{at} \quad z = 4,\ 6,\ 8,\ 10, \tag{A14}$$

respectively. These ratios apply at every halo mass at a given redshift for the multiplicative implementation adopted here.

The corresponding cumulative abundances are

$$n_{\rm ST}(>M_{\rm min},z)=\int_{M_{\rm min}}^{\infty}\frac{dn_{\rm ST}}{dM_h}(M_h,z)\,dM_h \tag{A15}$$

and

$$n_{\rm KST}(>M_{\rm min},z)=\int_{M_{\rm min}}^{\infty}\frac{dn_{\rm KST}}{dM_h}(M_h,z)\,dM_h. \tag{A16}$$

Since $F_{\rm K}(z)$ is independent of M_h in this prescription, it may be taken outside the mass integral, giving

$$\boxed{n_{\rm KST}(>M_{\rm min},z)=F_{\rm K}(z)n_{\rm ST}(>M_{\rm min},z)}. \tag{A17}$$

The same multiplicative relation holds for any mass-weighted integral over the halo mass function when the integration limits and all other assumptions are held fixed.

Finally, the calibration boundary of the adopted correction must be kept explicit. The Bolshoi-based fit is used quantitatively in this work only over the approximate interval

$$0\le z\le 10. \tag{A18}$$

Although equation (A11) can be evaluated mathematically at $z>10$, such values constitute an extrapolation of the fit rather than a calibrated KST prediction. Observational systems beyond $z=10$ may therefore be shown for context, but they are not used here as the basis for calibrated KST abundance constraints.

A.2. *Deterministic halo-to-UV mapping*

The halo mass function determines the abundance of halos, but an additional baryonic prescription is required to associate a halo of mass M_h with an observable rest-frame ultraviolet luminosity. We adopt the same deliberately simple deterministic mapping used in the main text so that the roles of halo abundance and baryonic conversion remain clearly separated.

The total baryonic mass associated with a halo is taken to be

$$M_b=f_bM_h, \tag{A19}$$

where

$$f_b=\frac{\Omega_b}{\Omega_m} \tag{A20}$$

is the cosmic baryon fraction (Planck Collaboration VI 2020; Boylan-Kolchin 2023). This is the maximum cosmological baryonic reservoir associated with the halo; it should not be interpreted as implying that all of the baryons are cold, retained, or available for immediate star formation.

We parameterize the stellar mass as

$$M_\star=\epsilon_\star(M_h,z)\,f_bM_h, \tag{A21}$$

where $\epsilon_\star$ is an effective stellar-conversion efficiency. The physical range satisfies

$$0<\epsilon_\star\le 1. \tag{A22}$$

The limiting value $\epsilon_\star=1$ represents an absolute baryonic ceiling in which the entire cosmological baryon allotment is converted into stars; it is not intended as a realistic galaxy-formation efficiency. In the baseline calculations $\epsilon_\star$ is treated parametrically, while more complete models may allow both halo-mass and redshift dependence (Behroozi *et al.* 2013; Moster *et al.* 2013; Somerville and Dav
'e 2015).

To obtain a characteristic star-formation rate, the stellar mass formed over the adopted timescale $t_\star$ is written as

$$\mathrm{SFR}(M_h,z)=\frac{\epsilon_\star(M_h,z)f_bM_h}{t_\star(z)}. \tag{A23}$$

For the first-order mapping used here, the timescale is parameterized as a fixed fraction of the Hubble time,

$$t_\star(z)=f_{\rm dyn}H^{-1}(z), \tag{A24}$$

where $f_{\rm dyn}$ is a dimensionless timescale parameter. Therefore

$$\mathrm{SFR}(M_h,z)=\frac{\epsilon_\star(M_h,z)f_bM_hH(z)}{f_{\rm dyn}}. \tag{A25}$$

This prescription should be understood as an effective time-averaged mapping, not as a detailed model of bursty star formation or gas accretion.

The corresponding intrinsic rest-frame UV spectral luminosity is taken to be

$$L_{\nu,\mathrm{UV}} = \kappa_{\mathrm{UV}}\,\mathrm{SFR}, \tag{A26}$$

where the baseline conversion adopted in the numerical calculations is

$$\kappa_{\mathrm{UV}} \simeq 8 \times 10^{27}\,\mathrm{erg\,s^{-1}\,Hz^{-1}}\,(M_\odot\,\mathrm{yr}^{-1})^{-1}. \tag{A27}$$

The precise value of κ_{UV} depends on assumptions concerning the stellar initial mass function, metallicity, stellar age, star-formation history, and population synthesis. It should therefore be regarded as part of the astrophysical mapping rather than a cosmological prediction (Bouwens *et al.* 2021; Finkelstein and Bagley 2022; Napolitano *et al.* 2025).

The AB absolute magnitude corresponding to a spectral luminosity $L_{\nu,\mathrm{UV}}$ is

$$M_{\mathrm{UV}} = 51.60 - 2.5\log_{10}\left(\frac{L_{\nu,\mathrm{UV}}}{\mathrm{erg\,s^{-1}\,Hz^{-1}}}\right). \tag{A28}$$

Combining the preceding relations gives the deterministic mean halo-to-magnitude mapping

$$\bar{M}_{\mathrm{UV}}(M_h, z) = 51.60 - 2.5\log_{10}\left[\frac{\kappa_{\mathrm{UV}}\,\epsilon_\star(M_h, z)\,f_b M_h H(z)}{f_{\mathrm{dyn}}}\right], \tag{A29}$$

where the quantities inside the logarithm are to be evaluated in mutually consistent units so that the argument represents the numerical value of $L_{\nu,\mathrm{UV}}$ in $\mathrm{erg\,s^{-1}\,Hz^{-1}}$.

Several features of equation (A29) are useful for interpreting the figures in the main text. At fixed redshift and fixed $\epsilon_\star$, increasing M_h increases the star-formation rate and UV luminosity and therefore produces a more negative, brighter M_{UV}. Likewise, increasing $\epsilon_\star$ shifts a halo of fixed mass toward brighter UV magnitude. The redshift dependence enters through $H(z)$ in the adopted star-formation timescale as well as through any explicit redshift dependence assigned to $\epsilon_\star$.

For the special baseline case in which $\epsilon_\star$ is independent of halo mass at fixed redshift, equation (A29) has the form

$$M_{\mathrm{UV}} = C(z, \epsilon_\star) - 2.5\log_{10} M_h, \tag{A30}$$

where $C(z, \epsilon_\star)$ contains the baryon fraction, UV conversion, star-formation timescale, and the unit conversion associated with the chosen mass unit. It follows that

$$\frac{dM_{\mathrm{UV}}}{dM_h} = -\frac{2.5}{\ln 10}\frac{1}{M_h} \tag{A31}$$

and hence

$$\boxed{\left|\frac{dM_h}{dM_{\mathrm{UV}}}\right| = \frac{\ln 10}{2.5}M_h}. \tag{A32}$$

This Jacobian is the factor required to transform the halo mass function into the deterministic UV luminosity function in the following subsection.

Most importantly, the mapping in this subsection is common to the ST and KST branches. The Klypin correction modifies the statistical abundance assigned to halos but does not alter M_b, $\epsilon_\star$, $t_\star$, κ_{UV}, or the luminosity assigned to an individual halo. Thus, at fixed $(M_h, z, \epsilon_\star)$,

$$M_{\mathrm{UV,ST}} = M_{\mathrm{UV,KST}}. \tag{A33}$$

The distinction between ST and KST appears only when the halo-to-light mapping is combined with their different halo abundances to construct a population luminosity function.

The deterministic prescription is intentionally a controlled baseline. It does not include scatter in luminosity at fixed halo mass, dust attenuation, bursty star formation, stochastic gas accretion, feedback, or AGN contamination. These effects can be incorporated through the conditional probability $P(M_{\mathrm{UV}} \mid M_h, z)$ introduced at the beginning of this Appendix and are considered in later subsections.

A.3. *Deterministic ST and KST luminosity functions*

The deterministic halo-to-UV relation derived in the preceding subsection allows the halo mass function to be transformed directly into a rest-frame UV luminosity function. Define

$$\Phi_X(M_{\mathrm{UV}}, z) \equiv \frac{dn_X}{dM_{\mathrm{UV}}}, \qquad X \in \{\mathrm{ST}, \mathrm{KST}\}, \tag{A34}$$

so that Φ_X has units of comoving number density per unit magnitude.

For a monotonic, single-valued mapping between M_h and M_{UV}, conservation of objects gives

$$\Phi_X(M_{\mathrm{UV}}, z)\;|dM_{\mathrm{UV}}| = \frac{dn_X}{dM_h}(M_h, z)\,dM_h. \tag{A35}$$

Therefore,

$$\boxed{\Phi_X(M_{\rm UV},z) = \frac{dn_X}{dM_h}(M_h,z)\left|\frac{dM_h}{dM_{\rm UV}}\right|\Bigg|_{M_h=M_h(M_{\rm UV},z)}} \tag{A36}$$

where the halo mass on the right-hand side is the mass corresponding to the specified UV magnitude under the adopted halo-to-light mapping.

For the ST branch,

$$\Phi_{\rm ST}(M_{\rm UV},z) = \frac{dn_{\rm ST}}{dM_h}\left|\frac{dM_h}{dM_{\rm UV}}\right|\Bigg|_{M_h=M_h(M_{\rm UV},z)}, \tag{A37}$$

whereas for the KST branch,

$$\Phi_{\rm KST}(M_{\rm UV},z) = \frac{dn_{\rm KST}}{dM_h}\left|\frac{dM_h}{dM_{\rm UV}}\right|\Bigg|_{M_h=M_h(M_{\rm UV},z)}. \tag{A38}$$

Using the multiplicative KST prescription from equation (A12),

$$\frac{dn_{\rm KST}}{dM_h} = F_{\rm K}(z)\frac{dn_{\rm ST}}{dM_h}, \tag{A39}$$

and using exactly the same halo-to-light mapping for both branches gives

$$\boxed{\Phi_{\rm KST}(M_{\rm UV},z) = F_{\rm K}(z)\,\Phi_{\rm ST}(M_{\rm UV},z)}. \tag{A40}$$

Thus, within the deterministic model adopted here, the KST correction changes the normalization of the predicted UV luminosity function at a given redshift but does not change its shape as a function of $M_{\rm UV}$. This result is a direct consequence of the assumed mass independence of $F_{\rm K}(z)$ and would not generally hold for a mass-dependent halo-mass-function correction.

For the baseline case used in the numerical luminosity-function calculation, $\epsilon_\star$ is independent of halo mass at fixed redshift. The halo-to-light relation then has the form

$$M_{\rm UV} = C(z,\epsilon_\star) - 2.5\log_{10}\left(\frac{M_h}{M_\odot}\right), \tag{A41}$$

where $C(z,\epsilon_\star)$ contains the adopted baryon fraction, star-formation efficiency, star-formation timescale, UV conversion factor, and the corresponding unit conversions. Differentiation gives

$$\frac{dM_{\rm UV}}{dM_h} = -\frac{2.5}{\ln 10}\frac{1}{M_h}, \tag{A42}$$

and therefore

$$\left|\frac{dM_h}{dM_{\rm UV}}\right| = \frac{\ln 10}{2.5}M_h. \tag{A43}$$

The corresponding deterministic luminosity functions become

$$\boxed{\Phi_{\rm ST}(M_{\rm UV},z) = \frac{\ln 10}{2.5}M_h\frac{dn_{\rm ST}}{dM_h}\Bigg|_{M_h=M_h(M_{\rm UV},z)}} \tag{A44}$$

and

$$\boxed{\Phi_{\rm KST}(M_{\rm UV},z) = \frac{\ln 10}{2.5}M_h\frac{dn_{\rm KST}}{dM_h}\Bigg|_{M_h=M_h(M_{\rm UV},z)}}. \tag{A45}$$

Both expressions have units of comoving number density per magnitude.

An important distinction follows from these equations. Changing $\epsilon_\star$ alters the relation between M_h and $M_{\rm UV}$ and therefore shifts the predicted luminosity function horizontally in magnitude space as well as changing which part of the halo mass function contributes at a specified luminosity. By contrast, at fixed redshift the adopted KST correction multiplies the ST luminosity function vertically by $F_{\rm K}(z)$. The two effects are therefore physically and mathematically distinct: $\epsilon_\star$ controls the baryonic halo-to-light mapping, whereas $F_{\rm K}$ controls the cosmological halo supply.

For the representative redshifts used in the population-level comparison, the vertical KST suppression is substantial. The values $F_{\rm K}(6) \simeq 0.496$, $F_{\rm K}(8) \simeq 0.265$, and $F_{\rm K}(10) \simeq 0.139$ imply that the deterministic KST luminosity function is approximately 49.6, 26.5, and 13.9 per cent of the corresponding ST prediction at those redshifts. Equivalently, ST predicts approximately 2.02, 3.77, and 7.18 times the KST abundance, respectively. These are the population-level differences illustrated in the ST/KST UV-luminosity-function comparison in the main text.

The deterministic luminosity function should be interpreted as a controlled baseline rather than a complete galaxy-formation prediction. It assumes a one-to-one relation between halo mass and UV magnitude and therefore neglects scatter, burstiness, dust attenuation, stochastic assembly histories, and other sources of variation at fixed halo mass. A more general treatment replaces the deterministic transformation with a conditional probability distribution $P(M_{\rm UV} \mid M_h, z)$, as developed in the following subsection.

A.4. *Including realistic scatter in the halo-to-light relation*

The deterministic mapping developed above assigns a single UV magnitude to each halo mass at fixed redshift. Real galaxies, however, need not obey a one-to-one halo–luminosity relation. Variations in star-formation history, gas accretion, merger history, metallicity, dust attenuation, feedback, halo assembly, and possible AGN contamination can produce a distribution of UV luminosities at fixed halo mass. A more general formulation therefore introduces the conditional probability distribution

$$P(M_{\rm UV} \mid M_h, z), \tag{A46}$$

normalized according to

$$\int_{-\infty}^{+\infty} P(M_{\rm UV} \mid M_h, z)\, dM_{\rm UV} = 1. \tag{A47}$$

A useful illustrative model is Gaussian scatter in UV magnitude about the deterministic mean relation $\bar{M}_{\rm UV}(M_h, z)$,

$$P(M_{\rm UV} \mid M_h, z) = \frac{1}{\sqrt{2\pi}\sigma_{\rm UV}} \exp\left[-\frac{\left[M_{\rm UV} - \bar{M}_{\rm UV}(M_h, z)\right]^2}{2\sigma_{\rm UV}^2}\right], \tag{A48}$$

where $\sigma_{\rm UV}$ denotes the intrinsic scatter in magnitude at fixed halo mass. Values of order

$$\sigma_{\rm UV} \sim 0.3\text{–}0.7 \text{ mag} \tag{A49}$$

may be used illustratively to explore the sensitivity of the bright end to stochasticity. These values are not fitted parameters in the present work and are not used in the baseline luminosity-function curves shown in the main text.

With scatter included, the luminosity function is no longer obtained from a simple Jacobian transformation. Instead,

$$\Phi_X(M_{\rm UV}, z) = \int_{M_{\rm min}}^{M_{\rm max}} \frac{dn_X}{dM_h}(M_h, z)\, P(M_{\rm UV} \mid M_h, z)\, dM_h, \qquad X \in \{\rm ST, KST\}. \tag{A50}$$

Thus,

$$\Phi_{\rm ST}(M_{\rm UV}, z) = \int_{M_{\rm min}}^{M_{\rm max}} \frac{dn_{\rm ST}}{dM_h}(M_h, z)\, P(M_{\rm UV} \mid M_h, z)\, dM_h, \tag{A51}$$

and

$$\Phi_{\rm KST}(M_{\rm UV}, z) = \int_{M_{\rm min}}^{M_{\rm max}} \frac{dn_{\rm KST}}{dM_h}(M_h, z)\, P(M_{\rm UV} \mid M_h, z)\, dM_h. \tag{A52}$$

For the particular KST prescription adopted in this work,

$$\frac{dn_{\rm KST}}{dM_h} = F_{\rm K}(z) \frac{dn_{\rm ST}}{dM_h}, \tag{A53}$$

and $F_{\rm K}(z)$ is independent of halo mass at fixed redshift. If the same conditional halo-to-light distribution $P(M_{\rm UV} \mid M_h, z)$ is adopted for ST and KST, the correction may therefore be taken outside the integral:

$$\begin{aligned}\Phi_{\rm KST}(M_{\rm UV}, z) &= F_{\rm K}(z) \int_{M_{\rm min}}^{M_{\rm max}} \frac{dn_{\rm ST}}{dM_h}(M_h, z) P(M_{\rm UV} \mid M_h, z)\, dM_h \\ &= \boxed{F_{\rm K}(z)\, \Phi_{\rm ST}(M_{\rm UV}, z)}.\end{aligned} \tag{A54}$$

Consequently, scatter can alter the shape of both luminosity functions while preserving their multiplicative ST/KST ratio at a fixed redshift under the assumptions used here.

The physical importance of scatter is greatest where the underlying halo mass function is steep. At the bright end, very massive halos are intrinsically rare, whereas somewhat lower-mass halos are much more numerous. A symmetric scatter in magnitude can therefore produce an asymmetric change in number counts: more objects can scatter from the numerous moderate-mass population into a rare bright bin than in the reverse direction. This is the familiar Eddington-like enhancement of a steeply declining distribution.

The effect can be represented schematically as

$$\Phi_{\rm bright}^{\rm scatter} > \Phi_{\rm bright}^{\rm deterministic} \tag{A55}$$

over portions of the bright tail, although the magnitude of the enhancement depends on $\sigma_{\rm UV}$, the local slope and curvature of the halo mass function, the mean halo-to-light relation, and the adopted mass integration limits. Scatter therefore cannot in general be represented by a single redshift-independent multiplicative factor.

This distinction is especially relevant at high redshift. A deterministic model may assign a very bright source only to an exceptionally massive and rare halo, whereas a stochastic model permits a more common lower-mass halo to occupy the same observed magnitude temporarily. Scatter can consequently reduce the severity of an apparent bright-end abundance discrepancy without requiring a corresponding increase in the abundance of the most massive halos.

However, this possibility should not be confused with the calculations actually presented in the main figures. The ST and KST UV luminosity functions used for the baseline population comparison in this work employ the deterministic mapping of the preceding subsections; no luminosity scatter is folded into those plotted curves. Equations (A50)–(A54) are included to show how the framework can be generalized and to identify one of the principal astrophysical uncertainties that should be incorporated in a future statistical analysis.

A fully developed implementation could allow $\sigma_{\rm UV} = \sigma_{\rm UV}(M_h, z)$ and could replace the Gaussian model with a non-Gaussian or physically generated conditional distribution. It could also include correlations among star-formation efficiency, dust attenuation, halo assembly history, and AGN contribution. Such extensions would modify the detailed luminosity-function shape, but as long as the same conditional mapping is applied to both ST and KST and the adopted $F_{\rm K}(z)$ remains mass-independent, their relative normalization at fixed redshift continues to be set by the Klypin factor.

A.5. *Duty cycle and occupation fraction*

The halo mass function specifies the abundance of dark matter halos, but not every halo necessarily hosts the luminous population under consideration, nor is every potential source observable at a given time. This distinction is particularly important for active galactic nuclei (AGN), whose observable number density depends on both the presence of a central black hole and the fraction of time for which that black hole is in an active, sufficiently luminous accretion state.

We describe these effects using a halo occupation fraction $f_{\rm occ}(M_h, z)$ and a duty cycle $f_{\rm duty}(M_h, z)$. The occupation fraction represents the probability that a halo of mass M_h at redshift z contains a black hole or other source belonging to the population of interest, whereas the duty cycle represents the probability that the source is active and observable during the relevant epoch. Both quantities satisfy

$$0 \le f_{\rm occ}(M_h, z) \le 1, \qquad 0 \le f_{\rm duty}(M_h, z) \le 1. \tag{A56}$$

For a threshold-based AGN host model in which only halos above $M_{\rm min}$ are capable of hosting the selected AGN population, the active AGN number density is

$$n_{{\rm AGN},X}(z) = \int_{M_{\rm min}}^{\infty} \frac{dn_X}{dM_h}(M_h, z)\, f_{\rm occ}(M_h, z)\, f_{\rm duty}(M_h, z)\, dM_h, \qquad X \in \{{\rm ST}, {\rm KST}\}. \tag{A57}$$

This expression makes explicit that halo abundance, black-hole occupation, and AGN activity are separate ingredients.

If $f_{\rm occ}$ and $f_{\rm duty}$ are approximated as mass-independent over the relevant halo range, equation (A57) reduces to

$$\boxed{n_{{\rm AGN},X}(z) = f_{\rm occ}(z)\, f_{\rm duty}(z)\, n_X(> M_{\rm min}, z)}. \tag{A58}$$

Because both fractions are bounded by unity,

$$n_{{\rm AGN},X}(z) \le n_X(> M_{\rm min}, z), \tag{A59}$$

so the cumulative halo abundance provides an absolute host-supply ceiling for a one-AGN-per-halo interpretation.

For the multiplicative KST prescription adopted in this work,

$$n_{\rm KST}(> M_{\rm min}, z) = F_{\rm K}(z)\, n_{\rm ST}(> M_{\rm min}, z). \tag{A60}$$

If the same occupation and duty-cycle prescription is applied to both halo mass functions, then

$$\boxed{n_{\rm AGN,KST}(z) = F_{\rm K}(z)\, n_{\rm AGN,ST}(z)}. \tag{A61}$$

Thus the KST correction reduces the available active-AGN population by the same redshift-dependent factor as the underlying halo population under these assumptions.

More generally, a luminosity-selected AGN population may be written using a conditional luminosity distribution,

$$\Phi_{{\rm AGN},X}(L, z) = \int \frac{dn_X}{dM_h}(M_h, z)\, f_{\rm occ}(M_h, z)\, f_{\rm duty}(M_h, z) \times P(L \mid M_h, z, {\rm active})\, dM_h. \tag{A62}$$

where $P(L \mid M_h, z, {\rm active})$ describes the luminosity distribution of an active source in a halo of mass M_h. In an AGN application this distribution may depend on the black-hole–halo relation, black-hole mass, Eddington-ratio distribution, radiative efficiency, obscuration, and bolometric correction. These ingredients are conceptually distinct from the cosmological halo abundance.

It is important not to confuse this AGN duty-cycle formalism with the galaxy UV luminosity-function calculation developed in the preceding subsections. The baseline galaxy UV luminosity functions in the main text are obtained by applying the deterministic stellar halo-to-UV mapping directly to the ST and KST halo mass functions. No separate AGN occupation fraction or AGN duty-cycle factor is applied to those galaxy luminosity-function curves. The quantities $f_{\rm occ}$ and $f_{\rm duty}$ instead enter the AGN host-supply constraints and any future AGN-specific luminosity-function calculation.

The occupation fraction is primarily connected to black-hole seeding and retention. At high redshift it may depend on whether black holes originate from stellar remnants, direct-collapse channels, or other seed populations, and on whether subsequent mergers or dynamical processes retain those black holes within their hosts (Volonteri 2010; Inayoshi *et al.* 2020). The duty cycle instead describes the episodic nature of accretion and may depend on gas supply, angular-momentum transport, mergers, feedback, and the luminosity threshold used to define an "active" source.

Consequently, an observed AGN abundance does not uniquely determine a halo mass. A low observed number density may reflect rare massive hosts, a low occupation fraction, a short duty cycle, or some combination of these effects. Conversely, explaining a large AGN abundance with very massive host halos can require occupation and duty-cycle factors approaching their physical upper limits. The abundance analysis in the main text uses this logic to identify combinations of $M_{\rm min}$, $f_{\rm occ}$, and $f_{\rm duty}$ that are compatible with the cosmological supply of halos.

The treatment adopted here is intentionally phenomenological. A more complete halo-occupation model could allow $f_{\rm occ}$ and $f_{\rm duty}$ to vary with halo mass and redshift and could distinguish central and satellite populations. Such extensions would be necessary for a detailed forward model of AGN luminosity functions and clustering. For the present purpose, however, the simple formulation isolates the key constraint: the observable active population cannot exceed the supply of suitable host halos once occupation and activity fractions are taken into account.

A.6. *Bright-end scatter and Eddington-bias-like effects*

The general role of scatter in the halo-to-light relation was introduced in Appendix A.4. Here we isolate its consequence for the bright end of the UV luminosity function, where the underlying halo abundance declines most rapidly. This subsection is intended as a physical interpretation of the scatter formalism rather than as an additional ingredient in the baseline luminosity-function curves presented in the main text.

At a fixed redshift, the number of moderate-mass halos is much larger than the number of very massive halos. If the UV luminosity at fixed halo mass has a finite dispersion, some of these more numerous moderate-mass systems can scatter temporarily toward brighter magnitudes. Although scatter may operate in both directions, the steep decline of the parent halo population means that the net effect can enhance the abundance in the rare bright tail. This is analogous to the familiar Eddington-bias effect that arises when a steep underlying distribution is convolved with observational or intrinsic scatter.

For either halo-mass-function prescription, the contribution to a bright magnitude interval is contained in the general convolution

$$\Phi_X(M_{\rm UV}, z) = \int \frac{dn_X}{dM_h}(M_h, z)\, P(M_{\rm UV} \mid M_h, z)\, dM_h, \qquad X \in \{\rm ST, KST\}. \tag{A63}$$

The bright-end enhancement therefore does not require the observed luminous object to occupy the halo mass assigned by a strictly deterministic halo-to-light relation. A somewhat lower-mass and more abundant halo may contribute to the same bright magnitude bin through the high-luminosity tail of $P(M_{\rm UV} \mid M_h, z)$.

It is useful to define the enhancement relative to the deterministic prediction as

$$\mathcal{E}_X(M_{\rm UV}, z) \equiv \frac{\Phi_X^{\rm scatter}(M_{\rm UV}, z)}{\Phi_X^{\rm det}(M_{\rm UV}, z)}. \tag{A64}$$

Over portions of the steep bright tail one generally expects $\mathcal{E}_X > 1$, although neither its magnitude nor its detailed dependence on $M_{\rm UV}$ is universal. The enhancement depends on the width and shape of the conditional luminosity distribution, the local slope and curvature of the halo mass function, the mean halo-to-light relation, dust and stellar population assumptions, and the adopted mass integration range. It should therefore not be represented by a single constant correction factor.

For the KST prescription used in this paper,

$$\frac{dn_{\rm KST}}{dM_h} = F_{\rm K}(z)\frac{dn_{\rm ST}}{dM_h}, \tag{A65}$$

where $F_{\rm K}(z)$ is independent of halo mass at fixed redshift. If the same conditional distribution $P(M_{\rm UV} \mid M_h, z)$ is used in both branches, equation (A63) immediately gives

$$\boxed{\Phi_{\rm KST}^{\rm scatter}(M_{\rm UV}, z) = F_{\rm K}(z)\, \Phi_{\rm ST}^{\rm scatter}(M_{\rm UV}, z)}. \tag{A66}$$

Thus scatter may substantially reshape and enhance the bright tail, but under the assumptions adopted here it does not erase the relative ST/KST abundance suppression. In fact, because the same scatter kernel is applied to both branches, their ratio at any fixed $M_{\rm UV}$ and z remains

$$\frac{\Phi_{\rm KST}^{\rm scatter}}{\Phi_{\rm ST}^{\rm scatter}} = F_{\rm K}(z). \tag{A67}$$

This result also implies that, under the present assumptions, the fractional bright-end enhancement produced by scatter is identical for ST and KST:

$$\mathcal{E}_{\rm KST}(M_{\rm UV}, z) = \mathcal{E}_{\rm ST}(M_{\rm UV}, z). \tag{A68}$$

The absolute KST number density nevertheless remains lower because the available halo reservoir has already been reduced by $F_{\rm K}(z)$.

The physical interpretation is therefore straightforward. Scatter can reduce the halo mass that would be inferred for an individual very luminous object under a deterministic mapping and can increase the predicted abundance of bright objects by drawing from a much larger reservoir of lower-mass halos. This may lessen an apparent bright-end abundance tension. It does not, however, create additional dark matter halos or remove the KST suppression of the underlying halo population.

No scatter correction or Eddington-bias adjustment is applied to the baseline ST and KST luminosity-function curves shown in the main text. Those curves retain the deterministic mapping described in Appendix A.2 and Appendix A.3. The discussion here instead identifies a physically motivated extension that should be included in future forward-modeling and statistical comparison with high-redshift luminosity function measurements. In such an analysis, intrinsic luminosity scatter should also be distinguished from observational uncertainties in measured fluxes, photometric redshifts, completeness corrections, and inferred number densities.

A.7. *Side-by-side numerical implementation of the ST and KST branches*

The numerical calculations evaluate the ST and KST predictions as parallel branches of the same underlying cosmological calculation. This is important because the KST prescription is applied only as a correction to the halo abundance; it does not replace or modify the common power spectrum, mass variance, peak-height calculation, or baryonic halo-to-light mapping.

The computational sequence may be summarized as follows.

1. Adopt the cosmological parameters
$$(\Omega_m, \Omega_b, \Omega_\Lambda, h, \sigma_8, n_s) \tag{A69}$$
used throughout the main calculation.

2. Construct the linear matter power spectrum at $z = 0$,
$$P(k, 0) = A_{\rm norm}\, k^{n_s} T^2(k), \tag{A70}$$
using the adopted transfer function and determine $A_{\rm norm}$ by requiring the calculated variance on the $8\,h^{-1}$Mpc scale to reproduce the adopted value of σ_8. The same normalized power spectrum is used for both ST and KST.

3. Construct the halo-mass grid and corresponding smoothing radii through
$$R(M_h) = \left(\frac{3M_h}{4\pi\bar{\rho}_m}\right)^{1/3}. \tag{A71}$$
The numerical mass interval must be sufficiently broad to cover all halo thresholds, cumulative integrals, and halo masses contributing to the plotted luminosity range. The precise grid limits and resolution are numerical choices rather than additional physical assumptions.

4. Compute the present-day mass variance,
$$\sigma^2(M_h, 0) = \frac{1}{2\pi^2}\int_0^\infty k^2 P(k, 0) W^2[kR(M_h)]\, dk, \tag{A72}$$
using the same spherical top-hat window and numerical k grid for both halo mass-function branches.

5. At each requested redshift, compute the flat-ΛCDM growth factor $D(z)$, normalized to
$$D(0) = 1, \tag{A73}$$
and then evaluate
$$\sigma(M_h, z) = D(z)\sigma(M_h, 0) \tag{A74}$$
and
$$\nu(M_h, z) = \frac{\delta_c}{D(z)\sigma(M_h, 0)}. \tag{A75}$$
The same $D(z)$, $\sigma(M_h, z)$, and $\nu(M_h, z)$ are supplied to the ST and KST calculations.

6. Evaluate the standard ST differential halo mass function,

$$\frac{dn_{\rm ST}}{dM_h}(M_h, z), \tag{A76}$$

and retain it as the unmodified baseline prediction.

7. Independently evaluate the Klypin factor

$$F_{\rm K}(z) = \frac{[5.501D(z)]^4}{1 + [5.500D(z)]^4}, \tag{A77}$$

and construct the second halo-abundance branch,

$$\frac{dn_{\rm KST}}{dM_h}(M_h, z) = F_{\rm K}(z)\frac{dn_{\rm ST}}{dM_h}(M_h, z). \tag{A78}$$

The ST array is stored independently from the KST array.

8. Compute the cumulative halo abundances independently,

$$n_X(> M_{\rm min}, z) = \int_{M_{\rm min}}^{\infty} \frac{dn_X}{dM_h}(M_h, z)\, dM_h, \qquad X \in \{\rm ST, KST\}, \tag{A79}$$

together with any mass-weighted cumulative quantities required by the baryonic-reservoir analysis. Because $F_{\rm K}$ is mass-independent in the adopted implementation, these arrays provide a direct numerical check of

$$\frac{n_{\rm KST}(> M_{\rm min}, z)}{n_{\rm ST}(> M_{\rm min}, z)} = F_{\rm K}(z). \tag{A80}$$

9. Apply the common deterministic halo-to-UV prescription to obtain

$$M_{\rm UV} = \bar{M}_{\rm UV}(M_h, z; \epsilon_\star), \tag{A81}$$

for each selected value of the stellar-conversion efficiency $\epsilon_\star$. This mapping is calculated independently of whether the halo abundance is labeled ST or KST.

10. For the baseline luminosity-function calculation presented in the main text, transform each differential halo mass function using

$$\Phi_X(M_{\rm UV}, z) = \frac{dn_X}{dM_h}\left|\frac{dM_h}{dM_{\rm UV}}\right|\Bigg|_{M_h = M_h(M_{\rm UV}, z)}, \qquad X \in \{\rm ST, KST\}. \tag{A82}$$

For the baseline mass-independent $\epsilon_\star$ mapping,

$$\left|\frac{dM_h}{dM_{\rm UV}}\right| = \frac{\ln 10}{2.5} M_h. \tag{A83}$$

No luminosity scatter, AGN occupation fraction, or AGN duty-cycle factor is included in these baseline galaxy UV luminosity-function curves.

11. Store the ST and KST luminosity functions separately and verify the diagnostic ratio

$$R_\Phi(M_{\rm UV}, z) \equiv \frac{\Phi_{\rm KST}(M_{\rm UV}, z)}{\Phi_{\rm ST}(M_{\rm UV}, z)}. \tag{A84}$$

For the mass-independent Klypin correction and identical halo-to-light mapping adopted here,

$$\boxed{R_\Phi(M_{\rm UV}, z) = F_{\rm K}(z)} \tag{A85}$$

throughout the numerically sampled magnitude range, apart from interpolation, finite-grid, and floating-point effects.

12. Repeat the calculation over the required redshift grid. Quantitative KST interpretation is restricted to the approximate Bolshoi calibration interval

$$0 \le z \le 10. \tag{A86}$$

Any evaluation at $z > 10$ is treated explicitly as an extrapolation.

Several internal consistency checks are useful for validating the numerical implementation. First, the $z = 0$ power spectrum should reproduce the adopted σ_8 normalization. Second, the same $\sigma(M_h, z)$ and $\nu(M_h, z)$ arrays must enter both the ST and KST branches. Third, at every fixed redshift the ratios

$$\frac{dn_{\rm KST}/dM_h}{dn_{\rm ST}/dM_h}, \qquad \frac{n_{\rm KST}(>M_h)}{n_{\rm ST}(>M_h)}, \qquad \frac{\Phi_{\rm KST}}{\Phi_{\rm ST}} \tag{A87}$$

should each reproduce $F_{\rm K}(z)$ wherever the corresponding numerical quantities are well resolved. These provide particularly direct diagnostics for detecting accidental changes in normalization, inconsistent interpolation, or unintended modification of the ST baseline.

For graphical comparisons, the ST and KST predictions should be evaluated on the same mass, magnitude, and redshift grids. Corresponding ST and KST curves for the same physical parameter value—for example the same redshift, $\epsilon_\star$, minimum halo mass, or duty cycle—should also be displayed with a common color and distinguished by line style. This plotting convention does not affect the numerical calculation, but it makes the physical ST–KST comparison unambiguous.

The scatter formalism developed in Appendix A.4 may be added as a separate extension by replacing the deterministic Jacobian transformation with the convolution

$$\Phi_X(M_{\rm UV}, z) = \int \frac{dn_X}{dM_h} P(M_{\rm UV} \mid M_h, z)\, dM_h. \tag{A88}$$

Likewise, AGN-specific predictions may subsequently include the occupation and duty-cycle factors described in Appendix A.5. These extensions should be kept separate from the deterministic baseline so that changes caused by the cosmological halo supply can be distinguished from changes caused by baryonic or AGN population modeling.

The resulting numerical architecture therefore preserves the complete calculation chain

$$\begin{aligned} P(k) &\to \sigma(M_h, z) \to \nu(M_h, z) \to \frac{dn_{\rm ST}}{dM_h} \\ &\to \frac{dn_{\rm KST}}{dM_h} \to n_X(>M_h, z) \\ &\to M_{\rm UV}(M_h, z) \to \Phi_X(M_{\rm UV}, z). \end{aligned} \tag{A89}$$

while isolating the Klypin correction to the halo-abundance step. This side-by-side construction is the numerical basis for the ST/KST comparisons presented in the main text.

A.8. *Physical interpretation of the ST–KST comparison*

The side-by-side ST and KST calculations are most useful when the different physical ingredients in the prediction are kept conceptually separate. In the framework adopted in this work, three principal levels enter the connection between cosmology and the observed high-redshift population:

$$\begin{aligned} \frac{dn_X}{dM_h}(M_h, z) \quad &\text{cosmological halo supply,} \\ \bar{M}_{\rm UV}(M_h, z; \epsilon_\star) \quad &\text{mean stellar halo-to-light mapping,} \\ P(M_{\rm UV} \mid M_h, z) \quad &\text{optional luminosity scatter and baryonic variability,} \end{aligned} \tag{A90}$$

where $X \in \{\rm ST, KST\}$.

For the deterministic galaxy UV calculation used as the baseline in this paper, the third ingredient is replaced by the single-valued relation $M_{\rm UV} = \bar{M}_{\rm UV}(M_h, z; \epsilon_\star)$. Number conservation then gives

$$\boxed{\Phi_X(M_{\rm UV}, z) = \frac{dn_X}{dM_h}(M_h, z) \left|\frac{dM_h}{dM_{\rm UV}}\right|\Bigg|_{M_h = M_h(M_{\rm UV}, z)}, \quad X \in \{\rm ST, KST\}.} \tag{A91}$$

This expression is the appropriate physical chain for the baseline galaxy UV luminosity functions presented in the main text. In particular, no AGN duty cycle or black-hole occupation fraction is inserted into these galaxy luminosity-function curves.

If intrinsic scatter in the stellar halo-to-light relation is introduced, the corresponding expression becomes

$$\boxed{\Phi_X(M_{\rm UV}, z) = \int \frac{dn_X}{dM_h}(M_h, z)\, P(M_{\rm UV} \mid M_h, z)\, dM_h}. \tag{A92}$$

The conditional probability distribution then describes baryonic variability at fixed halo mass, while the halo mass function continues to determine the cosmological supply of potential hosts.

The AGN abundance problem is related but physically distinct. For an AGN-selected population, the abundance additionally depends on whether a halo contains a black hole and whether that black hole is active at the epoch of observation. The corresponding host-supply expression is

$$n_{\mathrm{AGN},X}(z) = \int_{M_{\mathrm{min}}}^{\infty} \frac{dn_X}{dM_h}(M_h, z)\, f_{\mathrm{occ}}(M_h, z)\, f_{\mathrm{duty}}(M_h, z)\, dM_h. \tag{A93}$$

Thus f_{occ} and f_{duty} belong to the AGN population model and should not be conflated with the stellar halo-to-UV mapping used for the galaxy luminosity function.

This separation is important for interpreting the ST–KST comparison. Both branches begin with the same cosmological parameters, linear matter power spectrum, growth factor, mass variance, peak height, and collapse prescription entering the ST baseline. They also use the same baryonic mapping when a galaxy or AGN observable is assigned to a halo. The distinction between the two branches is isolated to the adopted simulation-calibrated abundance correction,

$$\boxed{\frac{dn_{\mathrm{KST}}}{dM_h}(M_h, z) = F_{\mathrm{K}}(z) \frac{dn_{\mathrm{ST}}}{dM_h}(M_h, z)}. \tag{A94}$$

Because $F_{\mathrm{K}}(z)$ is independent of halo mass in the prescription used here, the correction changes the normalization of the halo population at a fixed redshift without changing the mass dependence of the ST mass function. Consequently,

$$\frac{dn_{\mathrm{KST}}/dM_h}{dn_{\mathrm{ST}}/dM_h} = F_{\mathrm{K}}(z) \tag{A95}$$

at every resolved halo mass. The same factor propagates into any quantity that is a linear integral or deterministic transformation of the halo mass function, provided all other assumptions are held fixed.

For example,

$$n_{\mathrm{KST}}(> M_{\mathrm{min}}, z) = F_{\mathrm{K}}(z) n_{\mathrm{ST}}(> M_{\mathrm{min}}, z), \tag{A96}$$

and for the deterministic stellar UV mapping,

$$\Phi_{\mathrm{KST}}(M_{\mathrm{UV}}, z) = F_{\mathrm{K}}(z) \Phi_{\mathrm{ST}}(M_{\mathrm{UV}}, z). \tag{A97}$$

Likewise, if identical black-hole occupation and duty-cycle functions are used for the two branches,

$$n_{\mathrm{AGN,KST}}(z) = F_{\mathrm{K}}(z) n_{\mathrm{AGN,ST}}(z). \tag{A98}$$

These relations make the physical interpretation particularly transparent. Changing $\epsilon_\star$ modifies the mapping between halo mass and stellar UV luminosity. Changing M_{min} modifies which portion of the halo population is available to host a selected object. Changing f_{occ} or f_{duty} modifies the fraction of suitable halos that contribute to an AGN sample. Introducing σ_{UV} or a more general conditional distribution changes the spread of luminosity at fixed halo mass. By contrast, the ST–KST distinction modifies the cosmological abundance assigned to the same underlying halo population.

This separation also clarifies the meaning of an apparent discrepancy with high-redshift observations. A mismatch in luminosity at a given halo mass primarily probes the baryonic or black-hole mapping, whereas a mismatch in the number of available hosts probes the halo abundance and the population occupation assumptions. These effects can partially compensate one another in an observational comparison, but they represent physically different mechanisms and should therefore not be combined into a single phenomenological correction.

The interpretation is especially important toward high redshift, where $F_{\mathrm{K}}(z)$ decreases rapidly. Relative to the ST baseline, the KST branch therefore supplies fewer halos before any assumptions about stellar efficiency, black-hole occupation, duty cycle, or luminosity scatter are applied. Higher star-formation efficiency or favorable AGN activity parameters can make an individual halo more luminous or increase the fraction of halos appearing in an observed sample, but they cannot increase the underlying cosmological number of halos predicted by the adopted KST mass function.

The physical structure of the calculation can therefore be summarized schematically as

$$\boxed{\begin{aligned} P(k) \to \sigma(M_h, z) \to \nu(M_h, z) \to \frac{dn_X}{dM_h} \\ \to \text{halo-to-observable mapping} \\ \to \text{observable population.} \end{aligned}} \tag{A99}$$

Here the first line represents the cosmological halo supply, while the halo-to-observable mapping contains the baryonic and/or black-hole physics. For the present analysis, the principal purpose of carrying ST and KST side-by-side is therefore not to introduce two different galaxy-formation models, but to quantify how a change in the calibrated high-redshift halo supply propagates through otherwise identical astrophysical assumptions.

A.9. *Connection to JWST observations*

The purpose of the halo-to-light construction developed in this Appendix is to place the theoretical halo-abundance calculation in the same observable plane as high-redshift galaxy measurements. Rest-frame ultraviolet luminosity functions are particularly useful for this purpose because they constrain not only whether halos can produce galaxies of a given luminosity, but also whether the cosmological halo population is sufficiently abundant to reproduce the observed number density of such systems.

The baseline comparison in this work uses representative measurements of the high-redshift galaxy UV luminosity function from Franco *et al.* (2025), Donnan *et al.* (2023), and Donnan *et al.* (2024). These data provide population-level constraints spanning the cosmic-dawn regime and complement comparisons based on individual unusually massive or luminous JWST sources. The theoretical curves and observational measurements should nevertheless be regarded as a controlled first-order comparison rather than a formal statistical fit.

For each theoretical branch,

$$X \in \{\mathrm{ST}, \mathrm{KST}\}, \tag{A100}$$

the deterministic prediction is

$$\Phi_X(M_{\mathrm{UV}}, z) = \frac{dn_X}{dM_h}(M_h, z) \left| \frac{dM_h}{dM_{\mathrm{UV}}} \right| \Bigg|_{M_h = M_h(M_{\mathrm{UV}}, z)} . \tag{A101}$$

The observational comparison therefore probes two logically distinct requirements. First, the adopted baryonic mapping must assign sufficiently bright UV luminosities to halos of plausible mass. Second, the halo mass function must provide enough such halos to reproduce the measured number density.

This distinction is central to the interpretation of the JWST comparison. A model can reproduce the luminosity of an individual source by increasing the stellar-conversion efficiency or modifying the star-formation timescale, yet still fail to provide enough host halos. Conversely, a cosmology may provide an adequate number of halos while an adopted baryonic prescription produces galaxies that are systematically too faint. The luminosity-function comparison therefore helps separate a halo-supply problem from a halo-to-light-conversion problem.

In the present deterministic model, changing $\epsilon_\star$ modifies the mapping between M_h and M_{UV}. Larger $\epsilon_\star$ produces a larger stellar mass and star-formation rate at fixed halo mass and therefore a brighter, more negative M_{UV}. The resulting theoretical luminosity function is shifted relative to the observational points because a specified UV magnitude is then associated with a different part of the halo mass function.

By contrast, the KST correction acts directly on the halo abundance. Since

$$\frac{dn_{\mathrm{KST}}}{dM_h} = F_{\mathrm{K}}(z) \frac{dn_{\mathrm{ST}}}{dM_h} \tag{A102}$$

and the same deterministic halo-to-light relation is used for both branches,

$$\boxed{\Phi_{\mathrm{KST}}(M_{\mathrm{UV}}, z) = F_{\mathrm{K}}(z) \Phi_{\mathrm{ST}}(M_{\mathrm{UV}}, z)}. \tag{A103}$$

Thus the ST and KST curves at a common redshift and common $\epsilon_\star$ have the same deterministic shape in this implementation but different normalizations.

The population-level comparisons used in the main text are chosen to sample several redshifts at which the theoretical ST–KST difference becomes progressively more important. The COSMOS-Web analysis of Franco *et al.* (2025) provides a large-area JWST determination of the UV luminosity function over a broad high-redshift interval and is used for the lower-redshift comparison. The measurements of Donnan *et al.* (2023) provide UV-luminosity-function constraints extending from approximately $z \simeq 8$ into the very high-redshift regime, while the later PRIMER analysis of Donnan *et al.* (2024) provides an independent multifield determination extending through approximately $z \simeq 9$–15. These datasets therefore provide a useful observational benchmark for the redshift evolution predicted by the halo-based model.

The representative numerical values of $F_{\mathrm{K}}(z)$ are given in Equation (37) of Section 2.6.

Consequently, for identical baryonic assumptions the KST luminosity function is approximately 49.6, 26.5, and 13.9 per cent of the corresponding ST prediction at $z = 6$, 8, and 10, respectively. Equivalently, the ST prediction is approximately 2.02, 3.77, and 7.18 times larger. The increasing separation toward high redshift illustrates why the calibration of the halo mass function becomes increasingly important when interpreting cosmic-dawn number densities.

The comparison should not be interpreted as establishing a unique value of $\epsilon_\star$ or as a precision goodness-of-fit test of either halo mass function. The baseline theoretical curves omit several effects that can alter the observed UV luminosity function, including intrinsic luminosity scatter, bursty star formation, dust attenuation, mass- and redshift-dependent star-formation efficiency, feedback, halo assembly history, and possible AGN contamination. Observational measurements also carry uncertainties associated with sample selection, completeness, photometric and spectroscopic redshifts, survey volume, cosmic variance, lensing where relevant, and contamination.

Scatter is especially relevant at the bright end. As discussed in Appendices A.4 and A.6, a distribution $P(M_{\mathrm{UV}} \mid M_h, z)$ can allow more numerous moderate-mass halos to contribute to bright magnitude bins. Such scatter can increase the predicted bright-end abundance relative to a deterministic model. It is not included in the baseline curves used in the

present observational comparison and should therefore be treated as an important extension rather than as an implicit correction to the plotted results.

Similarly, the galaxy UV luminosity-function comparison should be distinguished from the AGN abundance constraints developed elsewhere in this work. The baseline UV luminosity functions use a stellar halo-to-light mapping and do not multiply the galaxy counts by an AGN occupation fraction or duty cycle. AGN-specific predictions require additional assumptions concerning black-hole occupation, accretion duty cycle, Eddington-ratio distributions, radiative efficiency, obscuration, and the relation between black-hole and halo mass.

The Bolshoi calibration boundary also remains important in the observational interpretation. Quantitative KST comparisons in this work are restricted to approximately

$$z \leq 10. \tag{A104}$$

JWST measurements at $z > 10$ remain highly informative for early structure formation and galaxy evolution, but evaluation of the same Klypin fitting expression beyond this range constitutes an extrapolation rather than a simulation-calibrated KST prediction. Such measurements should therefore be used to motivate new high-redshift numerical calibrations rather than to claim a calibrated KST discrepancy.

The observational logic of the framework can finally be summarized as

$$\boxed{\begin{aligned} P(k) &\to \sigma(M_h, z) \to \nu(M_h, z) \to \frac{dn_X}{dM_h} \\ &\to M_{\rm UV}(M_h, z; \epsilon_\star) \\ &\to \Phi_X(M_{\rm UV}, z) \to \text{JWST comparison.} \end{aligned}} \tag{A105}$$

The first line describes the cosmological halo supply, the second the stellar halo-to-light mapping, and the third the observable population comparison.

The main value of this construction is therefore diagnostic. It provides a transparent way to ask whether an apparent high-redshift discrepancy is driven primarily by the abundance of dark matter halos, by the efficiency with which their baryons produce UV light, or by astrophysical and observational effects not included in the deterministic baseline. As JWST surveys continue to improve the precision and dynamic range of high-redshift luminosity functions, this separation will allow increasingly stringent tests of both early galaxy formation and the underlying halo-abundance model.

This paper was built using the Open Journal of Astrophysics LaTeX template. The OJA is a journal which provides fast and easy peer review for new papers in the `astro-ph` section of the arXiv, making the reviewing process simpler for authors and referees alike. Learn more at http://astro.theoj.org.